Technische Universität München
Fakultät für Physik

Bachelor thesis in physics

Measuring $p\Lambda$ Correlations in $\pi^- + W$ Reactions at 1.7 GeV/c with HADES

Messung von $p\Lambda$-Korrelationen in $\pi^- + W$-Reaktionen bei 1.7 GeV/c mit HADES

Matthias Michael Zipper

October 16, 2015

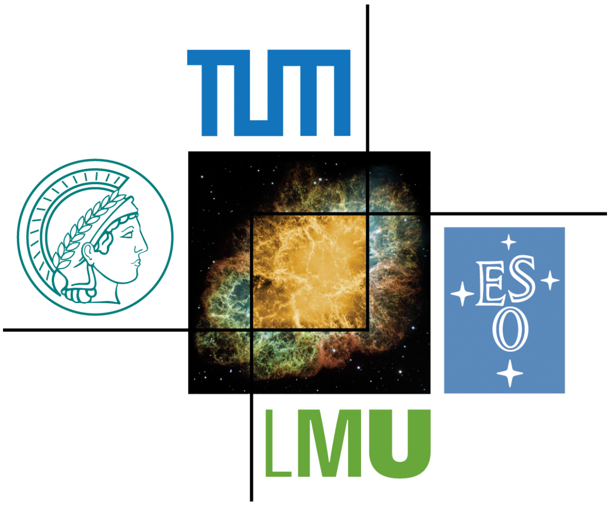

Supervisor:	Oliver Arnold
Primary reviewer:	Prof. Laura Fabbietti
Secondary reviewer:	PD Dr. habil. Andreas Ulrich

Contents

Chapter 1

Introduction

1.1 Motivation - Strange Particles in Neutron Stars

When a star's life comes to an end, it may explode into a supernova. The result of this massive last outburst mainly depends on the former object's mass. While heavy stars collapse into a black hole, stars of intermediate mass can form a neutron star, which is a very dense and very cold[1] astronomical object. The radius of neutron stars is typically around 10 km and they rotate at a rate of over 100 revolutions per second [1].

Because of their extreme properties, they are among the most interesting phenomena observed in astrophysics. Neutron stars serve as laboratories to examine matter under conditions that can hardly be implemented in earthbound experiments. Although they are subject to intensive ongoing research, their structure and the processes inside them are far from being entirely understood. An overview of what we already believe to know is given in Fig. 1.1.

Depending on their mass and rotation speed, neutron stars are thought to reach core densities up to a multiple of the normal nuclear density $\rho_0 \approx 2.48 \times 10^{14}$ g/cm^3, i.e. the average density of atomic nuclei in everyday matter [3]. Being the remains of an ordinary star, a young neutron star consists mainly of nucleons and electrons, all of which are fermions obeying Pauli's exclusion principle. Thus, it develops an enormous Fermi pressure, which prevents it from an ultimate gravitational collapse into a black hole.

At the same time, the Fermi pressure thermodynamically enables various subatomic processes mediated by the weak and strong interactions of the Standard Model[2]. Since it is inversely proportional to the mass of the considered particles[3], the light electrons feel the strongest urge to undergo transitions. They will perform inverse

---

[1] In the notion of a degenerate Fermi gas. Considering actual temperatures, it is extremely hot due to its high density.

[2] In this thesis, all statements are made under the assumptions of the Standard Model of particle physics. Physics beyond the Standard Model will *not* be discussed.

[3] The Fermi pressure P_F is given by $P_\mathrm{F} = \frac{h^2}{20m}\left(\frac{3}{\pi}\right)^{2/3}\rho^{5/3}$, where m is the mass of the particles forming the Fermi gas and ρ is their number density.

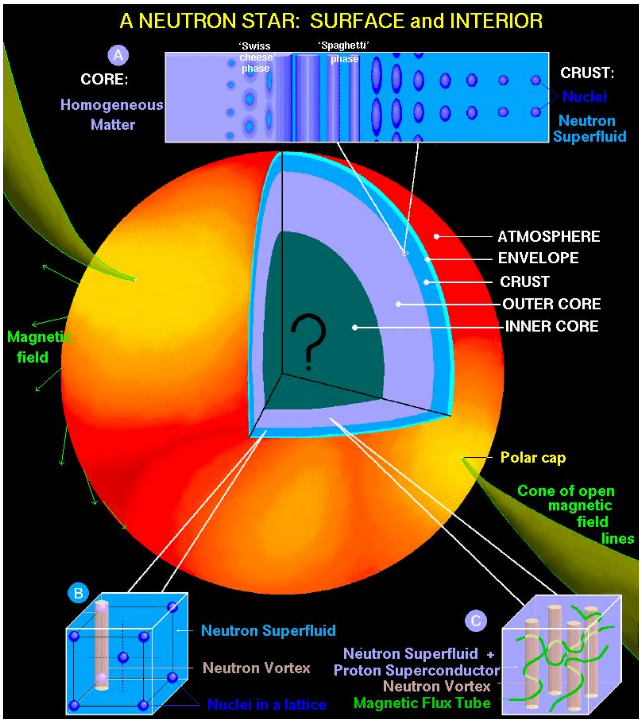

Figure 1.1: Artist's impression of the known structures inside neutron stars. The question mark suggests the existence of poorly understood processes in the core of the star. [2], [3]

β decays $e^- + p \rightarrow n + \nu_e$, where the neutrinos ν_e escape the star due to their evanescent mass and low likeliness to interact. As a consequence, the neutron star lowers its lepton number and accumulates the eponymous neutrons. However, the baryon number of the star stays basically the same. Since it is a fundamental conserved quantity, it cannot be changed by internal processes.

Closer to the core of the star, the pressure rises further. There will be almost no leptons left, so these regions can be described with a model of purely hadronic matter. This is usually achieved by combining nuclear physics and thermodynamics in order to develop an equation of state (EoS) of baryonic matter. Since an EoS depends on many parameters and assumptions, a multitude of competitive theories have emerged. Combining an EoS and general relativity provides a relation between size and mass of a neutron star, which are important observables in neutron star astronomy and offer a possibility to test the theories.

Most models of dense baryonic matter predict phase transitions for high temperatures or pressures. A simplified phase diagram is shown in Fig. 1.2. Apart from the actual transitions, the density-dependent occurrence of hyperons (i.e. baryons like

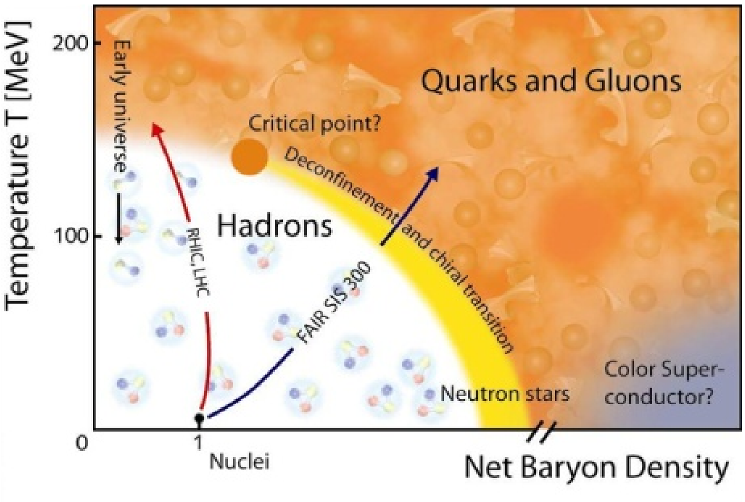

Figure 1.2: Simple phase diagram for baryonic matter. Ordinary atomic nuclei are located in the region of both low temperature and density. Neutron stars are still cold, but quite dense. [5]

Λ, Σ or Ξ which contain strange, but no heavier quarks; collective symbol Y) and baryon resonances (e.g. Δ) was hypothesized [4]. These particles are not stable in a vacuum, but can exist permanently in the extreme environment of a neutron star. They form individual Fermi gases and thus ease the Fermi pressure, providing a favorable configuration with lower energy. Their decay is inhibited, because there are no free quantum states available for daughter particles ("Pauli blocking"). The *order* of appearance of the different particle species (see Fig. 1.3) still strongly depends on the interactions between the particles, though.

The creation of new degrees of freedom through new particles is said to "soften" the equation of state, because it leads to a higher compressibility of the neutron star. As a consequence, the star will shrink, if it tries to accumulate more mass. This leads to an upper limit for the mass of the star, which depends on the assumptions of the considered model. Popular models with a rather soft EoS postulate a boundary around 1.5 solar masses ([4], see Fig. 1.4). However, astronomical observations have revealed the existence of neutron stars with 2 solar masses [1], which would require a "stiff" equation of state.

This conflict between theoretical predictions and experimental results is known as the "hyperon puzzle". To be able to discuss this problem, it is necessary to have detailed knowledge about the particles that are supposed to appear in dense baryonic matter and their interactions, both with particles of the same species and with others.

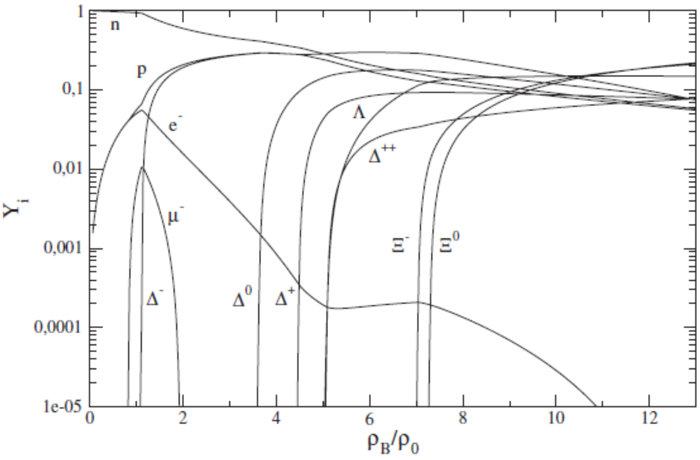

Figure 1.3: Particle fractions for baryon densities ρ_{B} up to $13\rho_0$. The successive occurrence of Δ resonances and hyperons (Λ, Ξ) generates new degrees of freedom. [4]

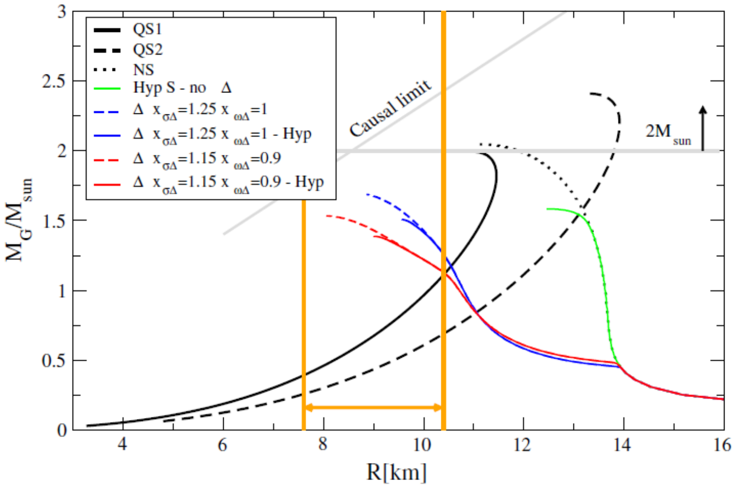

Figure 1.4: Several mass-radius relations from theoretical models. For soft equations of state with additional particles (colored curves), there is a mass limit well below the observed value of 2 solar masses. The green curve, which illustrates the sole occurrence of hyperons (i.e. there are no Δs), is in particular interesting for our analysis, since it demonstrates the “hyperon puzzle”. With neutrons only (dotted curve), theory would be able to reproduce the observed masses. [4]

1.2 Research Aim

Due to its neutral charge and relatively low mass, the Λ hyperon[4] might be a candidate for an early appearance in the row of additional particles in dense baryonic matter. However, this issue also depends on the forces that act upon a Λ while being embedded inside the interacting medium. We can imagine these interactions as an effective potential which adds[5] to the Λ mass to constitute the actual energy that is needed to create one particle. This is the relevant quantity for a thermodynamical description of the system.

The mean potential is derived from the interactions between the Λ and the other particles present in the medium. In the many-body system, the relationships are quite intricate, but some processes can be observed in a vacuum as well. The parameters of these isolated interactions can be calculated theoretically using different approaches. In this thesis, we execute an analysis on experimental data in order to assess a set of parameters of $p\Lambda$ interaction obtained from [6].

The data was collected with the HADES spectrometer located at GSI in Darmstadt, Germany, in a setup with a 1.7 MeV/c beam of π^- and a segmented tungsten (W) target. It is examined in a final state correlation analysis, where we will also obtain an estimate for the size of the $p\Lambda$ source. Furthermore, we test the applicability of the so-called “kinematic refit”, which is a mathematical tool for the analysis of particle reactions, on the reconstruction of inclusively produced Λ hyperons.

---

[4] See Sec. 3.1 for details.

[5] Attractive forces are represented by a negative potential, which effectively results in a subtraction.

Chapter 2

The HADES Experiment

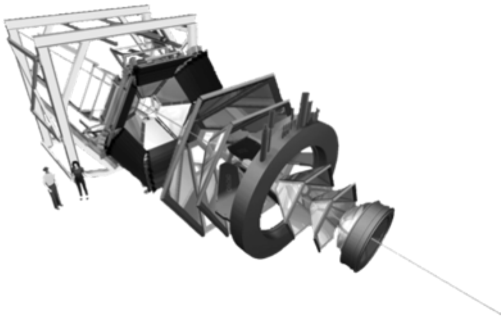

Figure 2.1: Exploded view of the HADES detector. The beam arrives from the bottom right and traverses the visible components RICH, MDC I and II, the magnet, MDC III and IV and the META system.

2.1 The HADES Experiment and Its Objective

The **H**igh **A**cceptance **Di**-**E**lectron **S**pectrometer HADES is a particle detector located at the GSI Helmholtzzentrum für Schwerionenforschung in Darmstadt, Germany. As its name suggests, it was primarily designed to measure electron-positron pairs. Creating a detector specialized on this particular task is motivated by the theoretical prediction that hadrons have different properties depending on whether they are in a vacuum or inside some strongly interacting medium. To provide such an environment, HADES is used in fixed target experiments. Short-lived hadronic particles like the light vector mesons ρ, ω and ϕ produced in particle reactions will decay mostly inside the target material, which allows us to test these theoretical in-medium models. While the daughter particles from their dominant hadronic decay modes are distorted themselves by the strongly interacting environment, the information about the rare electromagnetic decays of the mesons into an electron-positron pair (typical branching ratios[1] of $10^{-5} - 10^{-4}$) leaves the target almost unaltered. The precise measurement of these decays is the main objective of HADES.

Although it is optimized for detecting leptons, HADES is also capable of examining charged mesons and baryons, which can be either primary reaction products or daughter particles of short-lived intermediates. This is used to access other fields of hadron physics like the production of particles with strangeness (e.g. kaons and hyperons) and their behavior when embedded in a strongly interacting medium like an atomic nucleus.

The HADES program focuses mainly on heavy-ion experiments at beam energies of 1-2 GeV per nucleon. The required particle beams are provided by SIS18, GSI's 216 meter circumference heavy-ion synchrotron. Among the conducted experiments are ^{12}C+^{12}C, Ar+KCl and Au+Au. Additionally, there have been some elementary setups like proton-proton, deuterium-proton (both with a liquid hydrogen target), p+Nb and π^-+W (see Sec. 2.2.6).

2.2 Experimental Setup

This section describes the design of the HADES detector and the subcomponents used in our analysis. A more detailed explanation can be found in [8].

2.2.1 Basic Design

The HADES detector system has a sixfold symmetry, which is evident in Fig. 2.1. It is imposed by the use of six superconducting magnetic coils and following this principle, most parts of the detector consist of six identical segments that are arranged radially around the beam axis to give an almost full azimuthal coverage of about 85%. The longitudinal structure (see Fig. 2.2) is made up of several layers tilted towards the target region, all of which have their specific tasks that are explained below. This arrangement results in a large polar coverage from $\Theta = 18^\circ$ to $\Theta = 85^\circ$.

2.2.2 The Target

HADES is only used for fixed-target experiments. Because the moving center of mass of the reactions will usually make the particles move in a uniform longitudinal direction (which is the direction of the beam), the target is placed *in front* of the detector. The target also features a start detector, which gives the zero point for the reaction time measurement.

In the $\pi^- W$ setup for our analysis, the target consists of three tungsten foils in a row along the beam axis (cf. Sec. 4.1).

---

[1] All particle data (i.e. masses, mean lifetimes, branching ratios etc.) is taken from the Particle Data Group (PDG, [7]), unless otherwise specified.

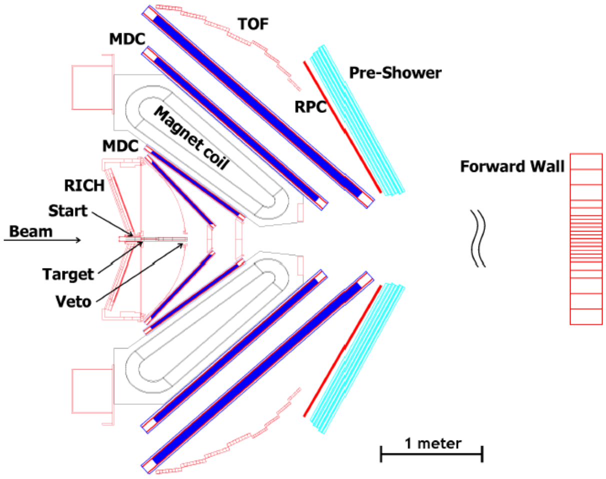

Figure 2.2: Longitudinal cross section of the HADES detector. As they do not play a role for this analysis, there will be no explanation about RICH and the Forward Wall. [9]

2.2.3 The Multi-wire Drift Chambers

The **M**ulti-wire **D**rift **C**hambers form (together with the magnet described below) the central part of the detector, which is responsible for the actual tracking and momentum determination of the particles. There are 24 trapezoidal MDC elements, which are arranged in four layers (I - IV) along the beam axis. As a consequence, every particle has to cross multiple elements, which is fundamental for reconstructing a particle track.
Each of the MDC elements consists of six layers of tungsten wires, which are tilted with respect to each other and embedded inside a chamber filled with a counting gas (see Fig. 2.3). If a charged particle traverses this gas, it will ionize some of the gas molecules and thus create free electrons. These electrons are accelerated by a voltage applied to the different layers of wires. The avalanche effect will then multiply the electrons, which leads to a measurable electric signal when they reach the wires. The amount of electrons can be related to the energy deposition $\mathrm{d}E$ inside the gas[2]. The position of the wires which gain the signal is used to determine a hit position.

2.2.4 The Magnet

The superconducting magnetic coils of the HADES detector are located between MDC II and III. They create a strong inhomogeneous toroidal field with up to

---

[2] Together with the flight distance $\mathrm{d}x$ inside the gas, this gives the energy loss $\mathrm{d}E/\mathrm{d}x$ of the particle.

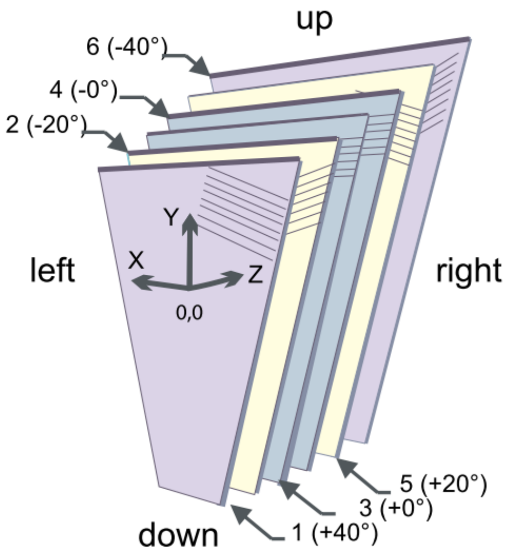

Figure 2.3: Schematic view of the arrangement of tungsten wires inside one MDC element. [8]

$B = 3.6$ T. Though, the region of the RICH, including the target, is almost field-free. Moving charged particles feel a Lorentz force inside the magnetic field. This will bend their tracks with a curvature inversely proportional to the particle momentum p.

As we only have up to four MDC hits, a major effort has to be put into reconstructing the particles' paths through the detector's "magnetic landscape". This is achieved by using the Runge-Kutta method to solve the equations of motion inside the field with sets of MDC hits as boundary conditions. Each fit result will both yield a track momentum and a χ^2 value, which is used in track sorting (see Sec. 4.2).

2.2.5 The Time-of-flight Detectors

There are three time-of-flight detectors in the HADES system, which form the **M**ultiplicity **E**lectron **T**rigger **A**rray (META): TOF, RPC (**R**esistive **P**late **C**hambers) and Pre-Shower. They represent the counter part to the start detector and allow a determination of the particle speed β. Furthermore, they may give an additional hit for momentum reconstruction.

Together with the momentum signal, the speed can be used to determine the particle mass according to special relativity:

$$m = p\sqrt{\frac{1}{\beta^2} - 1} \tag{2.1}$$

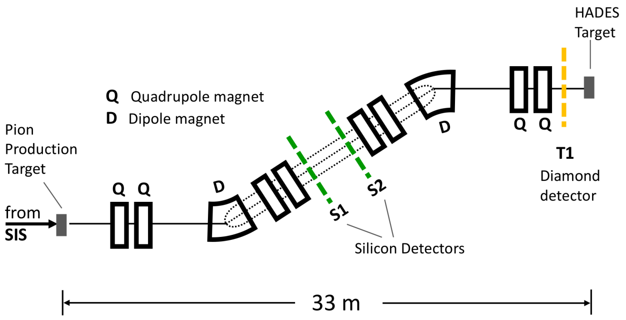

Figure 2.4: Beam line optics and tracking devices used in the preparation of the GSI pion beam. [10]

2.2.6 The Pion Beam

A special feature of the setup with which the analyzed experiment was conducted, is the fact that the π^- beam is a *secondary beam*. Since it is impossible to store pions for a longer period of time due to their instability, they have to be produced right before their use as beam particles. This is achieved with the pion production target, where ions from SIS18 impinge on beryllium (Be).

To select negative pions of the desired momentum from the variety of produced particles, sophisticated beam-line optics comprising dipole and quadrupole magnets are used. Furthermore, there is a pion tracking system to monitor the beam and improve the momentum resolution (see Fig. 2.4).

Chapter 3

Background and Theory

In the following sections, we want to give some background information about the physics examined in the correlation analysis. We will introduce the most important theoretical formulae and facts that will be needed in the experimental sections.

3.1 The Λ Baryon

In this section, we introduce some details about the Λ baryon, which plays a major role in our analysis and has already been mentioned in Ch. 1.

The Λ (Lambda) or Λ^0 particle is a neutral baryon with quark content uds. Because of the strange quark s, it is also referred to as the Λ *hyperon*. It can be found in the baryon octet or “Eightfold Way”, where it takes the role of the isospin singlet (see Fig. 3.1). It has a mass of $m_\Lambda = 1115.683(6)$ MeV and quantum numbers $I = 0$, $S = -1$ and $J^P = \frac{1}{2}^+$.
It is the lightest baryon with strange content and its mass difference to the lighter nucleons is below the kaon mass[1], so all of its decays have to violate the conservation

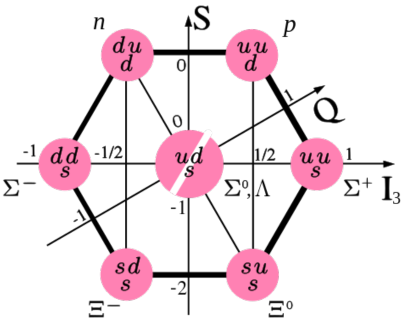

Figure 3.1: The baryon octet of flavor $SU(3)$. The Λ hyperon is an isospin singlet with one strange quark. [11]

---

[1] $\Delta m_{\Lambda n} = 176$ MeV, $\Delta m_{\Lambda p} = 177$ MeV, $m_{K^\pm} = 494$ MeV

Λ decay mode	branching ratio (Γ_i/Γ)
$p\pi^-$	63.9(5)%
$n\pi^0$	35.8(5)%

Table 3.1: The dominant decay modes for the Λ baryon and their branching ratios.

of strangeness which is granted for the strong and electromagnetic interaction. This means that there is no Λ decay that does not involve weak interactions, which are the only ones allowing a change of strangeness. Since these decays are rather slow, the Λ has a comparably large mean lifetime of $\tau_\Lambda = 2.632(20) \times 10^{-10}$ s[2], resulting in a $c\tau_\Lambda$ of 7.89 cm. Hence, a Λ will usually travel a macroscopically measurable distance before its decay, producing clearly distinct formation and decay vertices. This is going to play an important role in our analysis.

However, Λ baryons themselves cannot be detected with the HADES detector due to their electrical neutrality. Luckily, most of them decay before reaching the MDCs, dominantly into a pion and a nucleon, for which the branching ratios are given in Tab. 3.1. The neutral configuration $n\pi^0$ cannot be detected for the same reason, so about one third of the Λ signal is a priori lost, but the charged one can be measured inside the hadron sensitive part of the detector[3] and then used to reconstruct its mother particle (see Sec. 4.4).

3.2 Pion Nucleus Experiments and Strangeness Production

In this section, we want to give some information about the physics of pion (π) nucleus (A) collisions and the production of particles with strangeness $S \neq 0$ inside them.

An atomic nucleus is a complex bound state consisting of baryons called nucleons N (collective term for protons $p(uud)$ and neutrons $n(udd)$). They are held together by the strong force, but since they are color neutral hadrons, they will only interact by the exchange of mesons. While the isolated NN interaction is well understood (e.g. [12]), the description of the nucleus as a whole is a very challenging task, because there are too many particles for an analytic solution and too few for a statistical approach. These difficulties lead to the development of an own field, nuclear physics, which is subject to ongoing research until today.

---

[2] E.g. the Σ^0, which has a comparable mass of $m_{\Sigma_0} = 1192.642(24)$ MeV, only lives for $\tau_{\Sigma_0} = 7.4(7) \times 10^{-20}$ s on average, because it will almost always decay electromagnetically, $\Sigma^0 \to \Lambda^0 + \gamma$.

[3] With $c\tau_\pi$ being greater than 7 meters, charged pions are considered to be stable. This is a good approximation for our analysis.

Because of the complex structure of atomic nuclei, the description of their interactions is very challenging as well. A simple picture is that of a Fermi gas (or rather *two* Fermi gases, one for protons and one for neutrons), since all baryons, including nucleons, are fermions that obey Pauli's exclusion principle. If a particle ('bullet') travels through a nucleus ('target'), this "gas" can be treated as a rather homogeneous medium by the use of an effective model. Inside the target, the bullets motion is described via a mean potential accounting for the elastic scattering processes between the bullet and the nucleons. However, this model is only valid for bullet momenta $|\vec{p}_\mathrm{B}|$ that are much larger than the characteristic nucleon momentum, which is the Fermi momentum p_F.

In addition to elastic scattering, the bullet can also perform an inelastic reaction with one of the nucleons. This refers to processes, where not only energy and momentum of the particles are changed, but also their quantum numbers. Even entirely *new* particles can be produced. These processes have to be treated separately and can be calculated using quantum field theory.

In the case of our analysis, the bullet particle is a negative pion π^- and the target nucleus is tungsten (symbol W, proton number $Z = 74$, average nucleon number $A = 183.8$). We have no strangeness in the initial state, so a strange quark s can only occur, if there is a compensating anti-strange $\bar{s}$ as well. Since at our energy scale of $\sqrt{s} \approx 2$ GeV, we are well below the $\Lambda\bar{\Lambda}$ production threshold[4], the $\bar{s}$ quark has to be bound in a kaon, which can either be a $K^+(u\bar{s})$ or a $K^0(d\bar{s})$. We want to form a Λ, so we either have a neutral $(K^0\Lambda)$ or a positive $(K^+\Lambda)$ configuration in the final state. However, we can only have a negative $(\pi^- n)$ or a neutral $(\pi^- p)$ initial state, so additional negative pions may have to be produced in order to balance the charge. This leads to the basic reactions

- $\pi^- + p \to K^+ + \Lambda + \pi^-$,
- $\pi^- + p \to K^0 + \Lambda$,
- $\pi^- + n \to K^+ + \Lambda + \pi^- + \pi^-$ and
- $\pi^- + n \to K^0 + \Lambda + \pi^-$.

If there is enough energy available, there can still be more pions, provided that they have neutral charge (e.g. π^0 or $\pi^+\pi^-$). The dominant appearance of *negative* pions supports the abundance of π^- in our experimental data (see Sec. 4.1).

The actual mechanisms of strangeness production is shown in Fig. 3.2 using the example of the simple $\pi^- + p \to K^0 + \Lambda$ reaction. There can be several different intermediate nucleon resonances N^*, each giving their own contribution. The most

---

[4] A $\Lambda\bar{\Lambda}$ pair has baryon number $B = 0$, but there is always one baryon in the initial state ($B = 1$). Thus, we would need energy for at least three (anti-)baryons in the final state, ≈ 3 GeV.

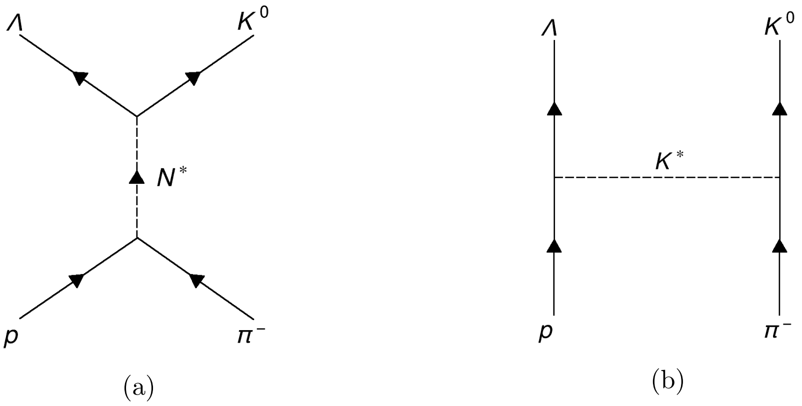

Figure 3.2: Strangeness production using the example of the reaction $\pi^- + p \rightarrow K^0 + \Lambda$. There is either an intermediate nucleon resonance N^* formed, which then decays into the strange particles, or proton and pion exchange a K^*.

$N^*(m/\mathrm{MeV})$	$\Gamma(N^* \rightarrow K\Lambda)/\Gamma_{\mathrm{tot}}$
$N(1650)$	3-11%
$N(1710)$	5-25%
$N(1720)$	1-15%
$N(1900)$	0-10%

Table 3.2: List of nucleon resonances with decay channels into a kaon and a Λ. The line-up is not exhaustive, but represents the most important candidates for our energy range ($\sqrt{s} \approx 2$ GeV).

important representatives for our energy range with notable branching ratios into $K\Lambda$ are listed in Tab. 3.2. For the K^*, there is usually only one diagram regarded, which is the $K(892)$.

Both the Λ and the K will be produced with a considerable momentum. As a Λ hyperon is not very strongly bound inside a nucleus (typical binding energies are of the order of few MeV [13]), it will usually escape, generating a potential event for our analysis[5].

The weak binding also allows other nucleons to leave the nucleus, if they get a sufficient kick from elastic scatterings. If a proton is freed in a Λ event, both particles can fly alongside for some distance. Their interaction will generate some correlation, which will be examined in this analysis.

---

[5] A decay of the Λ into the detectable $p\pi^-$ channel is still necessary.

3.3 General Scattering Theory

This section deals with the basics of scattering and lays the foundation for understanding the following two sections.

In classical physics, the term "scattering" refers to the phenomenon that waves (light, sound, water waves etc.) can be forced to deviate from a straight line by some object or geometry. In particle physics, however, the notion of scattering is much more general, applying to virtually every interaction between particles. This association originates at the very roots of quantum mechanics, when Louis de Broglie hypothesized in 1924 that matter, i.e. particles, can exhibit wave-like behavior [14]. Since then, this idea has developed a lot. In 1950, Lippmann and Schwinger published an equation which provides stationary solutions for a free, non-relativistic particle of mass m with momentum $\vec{p}$, $p \equiv |\vec{p}|$ (modeled as a plane wave function $\phi_{\vec{p}}(\vec{x})$) being elastically scattered by some local potential $V(\vec{x}')$. It is an integral equation for the total wave function $\psi(\vec{x})$ that has to be solved self-consistently: [15]

$$\psi(\vec{x}) = \phi_{\vec{p}}(\vec{x}) - 2m \int \mathrm{d}^3x' \, \frac{\mathrm{e}^{\mathrm{i}p|\vec{x}-\vec{x}'|}}{4\pi|\vec{x}-\vec{x}'|} V(\vec{x}')\psi(\vec{x}') \tag{3.1}$$

For a large distance $r \equiv |\vec{x}|$ of the observer (compared to the extent of the potential $V(\vec{x}')$, thus $r \gg |\vec{x}'|$), we can approximate the solution by [16]

$$\begin{aligned} \psi(\vec{x}) &= \phi_{\vec{p}}(\vec{x}) - \frac{2m}{4\pi}\frac{\mathrm{e}^{\mathrm{i}pr}}{r} \int \mathrm{d}^3x' \mathrm{e}^{-\mathrm{i}\vec{p}'\cdot\vec{x}'} V(\vec{x}')\psi(\vec{x}') \\ &= \frac{1}{(2\pi)^{3/2}} \left(\mathrm{e}^{\mathrm{i}\vec{p}\cdot\vec{x}} + \frac{\mathrm{e}^{\mathrm{i}pr}}{r} f(p,\theta) \right), \end{aligned} \tag{3.2}$$

where $\vec{p}'$ is the momentum with which the scattered particle flies towards the spectator, i.e. $\vec{p}' = |\vec{p}|\frac{\vec{x}}{r}$. Hence, we can see that the scattering process basically turns the incoming plane wave into an outgoing spherical wave. The measured distribution of final state particles[6] depends on this superposition, which is governed by the complex coefficient $f(p,\theta)$, called the "scattering amplitude" (θ gives the deviation of the particle from $\vec{p}$ to $\vec{p}'$). With this scattering amplitude, it is easy to obtain the differential cross section of the scattering process via

$$\frac{\mathrm{d}\sigma}{\mathrm{d}\Omega} = |f(p,\theta)|^2 \, . \tag{3.3}$$

Because the full solution of a scattering problem can still be very tedious, another mathematical technique was developed, the partial wave analysis. It takes advantage

---

[6] Of course, we cannot determine the whole distribution from one single particle. Instead, we use a sufficiently large ensemble of identically prepared particles.

of the fact that the orbital angular momentum L of a two-body system (the incoming particle and the scatterer) is quantized in multiples of $\hbar$, represented by the quantum number $l \geq 0$. The incoming wave is decomposed into the corresponding angular momentum components, called "partial waves". The scattering problem can then be solved for each l independently to obtain partial-wave amplitudes $f_l(p)$. These now give an expansion for the total scattering amplitude [16]

$$f(p,\theta) = \sum_{l=0}^{\infty} (2l+1) f_l(p) P_l\left(\cos(\theta)\right). \tag{3.4}$$

Furthermore, the partial-wave amplitudes themselves can be expressed in terms of a phase shift $\delta_l(p)$:

$$f_l(p) = \frac{\mathrm{e}^{\mathrm{i}\delta_l(p)} \sin \delta_l(p)}{p} \tag{3.5}$$

An important parameter for experimental measurements is the "scattering length" f_0, which is the limit of the $l = 0$ partial-wave amplitude (usually referred to as the s-wave amplitude) for low momenta[7]:

$$f_0 \equiv - \lim_{p \to 0} f_0(p) \tag{3.6}$$

3.4 Correlation functions

In this section, we introduce the concept of correlation functions, which is an important part of our experimental analysis.

Back in 1956, Hanbury Brown and Twiss (HBT) published an experimental method called *intensity interferometry* [17]. They used it to correlate the signals of two spatially separated detectors measuring photons from a very distant, extra-terrestrial light source (e.g. a star). In doing so, they could extract information about the (angular) size of the source, which would not have been possible with conventional methods of astronomy.

The important aspect of the HBT approach is the examination of correlations between two *distinct* particles, in contrast to the well-known *amplitude interferometry*, which is based on the autocorrelation of *one* particle and can be demonstrated with the famous double-slit experiment. This fundamental difference is depicted schematically in Fig. 3.3.

More in detail, the measured quantities for intensity interferometry are the two-particle coincidence yield n_{12} and the single particle yields n_1 and n_2. If both

---

[7] In our analysis, a positive scattering length represents an attractive interaction. However, some authors use the opposite sign convention.

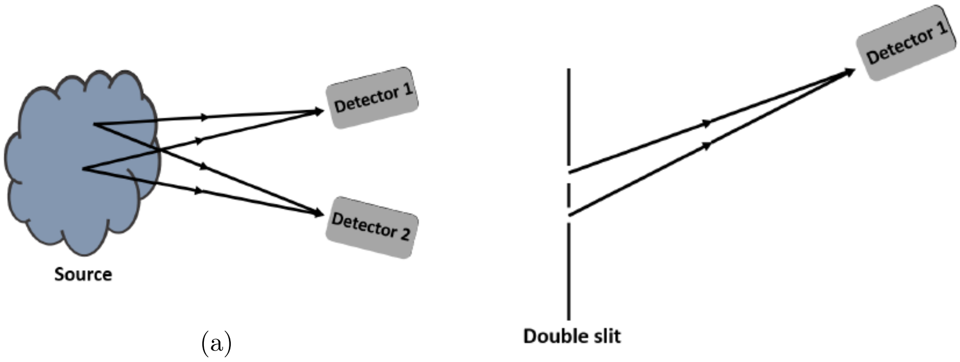

(a)

(b)

Figure 3.3: Illustration of the two kinds of interferometry.
Intensity interferometry (left) correlates the signals of two distinct particles from the same source. Amplitude interferometry (right) correlates the wave function of *one* particle with itself.

particles were entirely uncorrelated, the average $\langle n_{12} \rangle$ would factorize into the product $\langle n_1 \rangle \langle n_2 \rangle$. Hence, the quantity

$$C(\vec{p}_1, \vec{p}_2) = \frac{\langle n_{12} \rangle}{\langle n_1 \rangle \langle n_2 \rangle} \tag{3.7}$$

is called a “correlation function”, because its deviation from 1 indicates some correlation between the particles. This correlation is caused by the particles’ interactions on their way to the detector. By fitting experimental data with some theoretical model for $C(\vec{p}_1, \vec{p}_2)$, it is therefore possible to extract properties of the source and of the interaction.

In 1960, Goldhaber et al. independently discovered a similar effect, however, among like sign pions $\pi^{\pm}\pi^{\pm}$ in a particle physics experiment [18]. They were able to explain their results using Bose-Einstein statistics, which describes the symmetrization of the collective wave function of identical bosons (e.g. pions), introducing another effect that has to be taken into account for correlation functions. The applicability of the HBT effect on particle reactions opened an entire new field in nuclear and particle physics, which is known today as “femtoscopy”. The name illustrates the capability to resolve events down to the fermi scale ($\sim 10^{-15}$ m).

The full quantum mechanical description of two-particle correlation functions, which is essential for applications in particle physics, was developed in 1977 by Koonin and Pratt [19]. It involves the so-called “source function” $g(\vec{p}, x)$, which gives a measure for the probability that a particle with momentum $\vec{p}$ is emitted at the space-time point $x = (t, \vec{r})^T$. In terms of the total pair momentum $\vec{P}$ and the relative momentum

$\vec{q}$ in the pair's center of momentum frame, the universal Koonin-Pratt two-particle correlation function reads:

$$C\left(\vec{P},\vec{q}\right)=\frac{\int \mathrm{d}^4x_1\mathrm{d}^4x_2 g\left(\vec{P}/2,x_1\right)g\left(\vec{P}/2,x_2\right)\left|\phi\left(\vec{q},\vec{r}_1-\vec{r}_2-\frac{t_1-t_2}{2m}\vec{P}\right)\right|^2}{\int \mathrm{d}^4x_1 g\left(\vec{P}/2,x_1\right)\int \mathrm{d}^4x_2 g\left(\vec{P}/2,x_2\right)} \tag{3.8}$$

The relative wave function $\phi\left(\vec{q},\vec{r}_1-\vec{r}_2-\frac{t_1-t_2}{2m}\vec{P}\right)$ contains all interactions of the particles and has to be derived problem-specific. However, this model is only valid under certain assumptions, for instance the independence of successive emission processes and the negligibility of interactions between particle and source after the emission.

3.5 $p\Lambda$ Scattering and Correlation Function (Lednický-Lyuboshits model)

This section gives the most important properties of $p\Lambda$ interaction and finally introduces the theory function used in our experimental correlation analysis.

As already mentioned in Sec. 3.2, baryons are color-neutral objects, which prevents them from interacting via the exchange of gluons. Furthermore, Λ has no electrical charge, so electromagnetic interaction does neither play a role. Thus, disregarding any weak processes, the only contribution to elastic $p\Lambda$ scattering arises from the exchange of mesons. This mechanism, however, is a very complex superposition of many individual processes ("Feynman diagrams"). It is beyond the scope of this thesis to cover this topic to its full extent, but we will give a brief insight. A detailed treatment can be looked up in [20].

The most basic processes (leading order, LO) apart from contact interactions are one-meson exchanges. There are two possibilities for the $p\Lambda$ system (see Fig. 3.4), one with an exchange of strangeness (K meson, p and Λ "swap places") and one without (η meson). There can be no π exchange, since Λ is an isospin singlet.

The next order in the perturbation series (NLO) consists of two-meson exchanges. Because now virtual intermediate baryons come into play, the number of contributing diagrams rises drastically. The general configurations ("master diagrams") for exchanging two mesons are depicted in Fig. 3.5. However, the full set with labeled propagators will not be shown due to the sheer number of diagrams. In addition to kaons and η mesons, now also pions appear. As the Λ is located in the center of the flavor $SU(3)$ octet (see Fig. 3.1), all eight spin-1/2 baryons will occur. Furthermore, there are also contributions from the spin-3/2 decuplet, where all but the Δ^- and

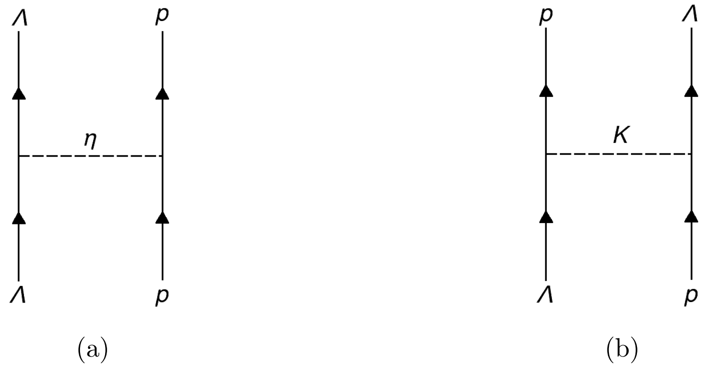

Figure 3.4: One-meson exchange diagrams for $p\Lambda$ scattering. The η meson (left) leaves the baryons unchanged, whereas the K leads to an exchange of strangeness. Pions cannot appear due to $I_\Lambda = 0$.

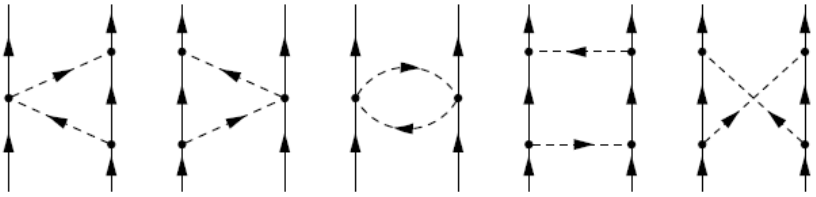

Figure 3.5: Master diagrams for the two-meson exchange. For $p\Lambda$ scattering, these diagrams describe the next-to-leading order (NLO) in the perturbation series. [20]

the Ω^- baryon can be reached.

From these theoretical considerations, the fundamental parameters of $p\Lambda$ interaction can be calculated, which are the scattering lengths f_0^S (cf. Eq. 3.6) and effective ranges d_0^S of the potential. Since we are dealing with spin-1/2 baryons, we have to take different spin configurations into account, i.e. three triplets ($S = 1$) and a singlet state ($S = 0$). The values we will use for our analysis are taken from [6] and displayed in Tab. 3.3. It has yet to be mentioned that the theoretical calculations for these values are in turn dependent on the parameters of the underlying theory, which have themselves to be obtained from scattering experiments.

For small one particle momenta $k \equiv \frac{1}{2}|\vec{q}|$ in the pair center of momentum frame, the dominant contribution to the scattering amplitude will come from the s-wave. Thus, it can be expressed in an effective range approximation as [21]

$$f^S(k) = \left(\frac{1}{f_0^S} + \frac{1}{2} d_0^S k^2 - \mathrm{i}k \right)^{-1} . \tag{3.9}$$

Under the assumption that proton and Λ are emitted with low time separation and

total spin	parameter	value
$S=0$	f_0^0	2.91 fm
	d_0^0	2.78 fm
$S=1$	f_0^1	1.54 fm
	d_0^1	2.72 fm

Table 3.3: Parameters of $p\Lambda$ interaction. Only s-wave contributions are listed, both for total spin $S=0$ and $S=1$. The listed values have been calculated in [6] using NLO chiral effective field theory.

the spatial source is a Gaussian distribution in the space separation $\vec{r}^*$

$$g(\vec{r}^*) \sim \exp(-\vec{r}^{*2}/4r_0^2), \tag{3.10}$$

the parameter r_0 can be considered as the effective size of the source, from which the Λ and the proton are emitted.

Lednický and Lyuboshits derived an analytical solution for the $p\Lambda$ correlation function [22]:

$$\begin{aligned} C(k) = 1 + \sum_S \rho_S \Bigg[& \frac{1}{2}\left|\frac{f^S(k)}{r_0}\right|^2 \left(1 - \frac{d_0^S}{2\sqrt{\pi}r_0}\right) \\ & + \frac{2\,\mathrm{Re}\, f^S(k)}{\sqrt{\pi}r_0} F_1(2kr_0) - \frac{\mathrm{Im}\, f^S(k)}{r_0} F_2(2kr_0) \Bigg] \end{aligned} \tag{3.11}$$

with $F_1(z) = \int\limits_0^z \mathrm{d}x e^{x^2-z^2}/z$ and $F_2(z) = (1-\mathrm{e}^{-z^2})/z$. ρ_S gives the fraction of $p\Lambda$ pairs with total spin S, which is $\rho_0 = 1/4$ and $\rho_1 = 3/4$ for unpolarized particle production. In Fig. 3.6, this theory function is shown for different source sizes for the set of parameters given in Tab. 3.3.

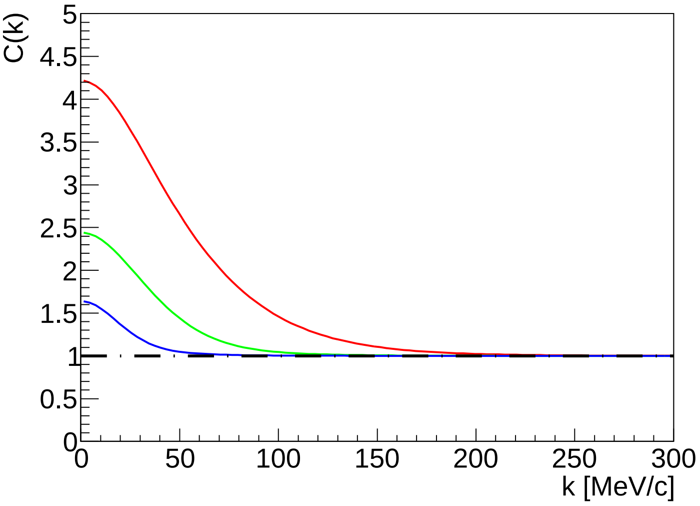

Figure 3.6: Example plots of the Lednický-Lyuboshits model for different $p\Lambda$ source sizes r_0. (red = 1 fm, green = 2 fm, blue = 4 fm)

Chapter 4

Experimental methods

This chapter describes the experimental techniques we use in our analysis. It contains all intermediate results and leads to the final results which will be discussed in Ch. 5.

4.1 General Information about the Dataset

A summary of information about the dataset analyzed in this thesis is given in Tab. 4.1. However, it anticipates some of the procedures which will be explained in the following sections. To understand the target geometry, the experimental primary vertex distribution in Fig. A.2 may come in handy.

beamtime		5 Jul till 11 Jul 2014
beam	particles	π^-
	momentum	1.7 GeV
target	material	${}^{183.8}_{74}W$ (tungsten)
	diameter	12 mm
	segment length	2.4 mm
	segment positions	-51.5 mm, -33.5 mm, -15.5 mm
center of mass energy $\sqrt{s}$		≈ 2 GeV
number of events		74845422
average number of ... per event	tracks	2.30
	sorted tracks	1.66
	identified particles	1.18
	protons	0.72
	π^+	0.13
	π^-	0.33
	Λ candidates	0.14

Table 4.1: Summary of the analyzed data set.

4.2 Track Sorting

As already mentioned in Ch. 2, the HADES detector was primarily designed for the precise measurement of leptons. However, in our analysis we need to determine the properties of pions and protons, which are hadrons. Because of that, we cannot use the hadron blind RICH detector, but have to rely on the universal MDCs. From Sec. 2.2.4, we know that the MDC detector hits are connected to tracks by using the Runge-Kutta method to solve the equations of motion inside the magnetic field. Still though, there may be tracks sharing ambiguous detector hits, of which only one is thought to be real.

The discrimination of fake tracks and a preliminary differentiation between leptons and hadrons is performed by the track sorter provided by the HYDRA framework of GSI [23]. It evaluates the product of the χ^2 value of the Runge-Kutta result and a number called "META match quality", which rates how well a possible hit in the META system (see Sec. 2.2.5) fits into the MDC track.

All further analysis steps are conducted after the application of the sorter. Events with no track accepted by the sorter are rejected. This is in particular important for this analysis, because tracks sharing a detector hit will obviously resemble each other in their momentum or spatial properties. Including such fake correlations would severely deteriorate our result.

4.3 Particle Identification

With the magnet and MDC information about the momentum p, polarity q and energy loss $\mathrm{d}E/\mathrm{d}x$ of the particles, we can create a histogram like the one displayed in Fig. 4.1. In this diagram, we can see peculiar, bend shaped structures, which can be understood using theoretical considerations about the energy loss of fast particles in a homogeneous medium. This phenomenon was treated by Bethe and Bloch, resulting in their famous relativistic Bethe-Bloch formula [24]

$$-\left\langle \frac{\mathrm{d}E}{\mathrm{d}x} \right\rangle = 4\pi N_{\mathrm{A}} r_e^2 m_e z^2 \frac{Z}{A}\frac{1}{\beta^2}\left[\ln\left(\frac{2m_e\beta^2\gamma^2 T_{\max}}{I^2}\right) - \beta^2 - \frac{\delta}{2}\right], \tag{4.1}$$

with the notations:

z: charge of the impinging particle

Z, A: proton and mass number of the material's atoms

m_e: electron rest mass

r_e: Bohr radius of the electron

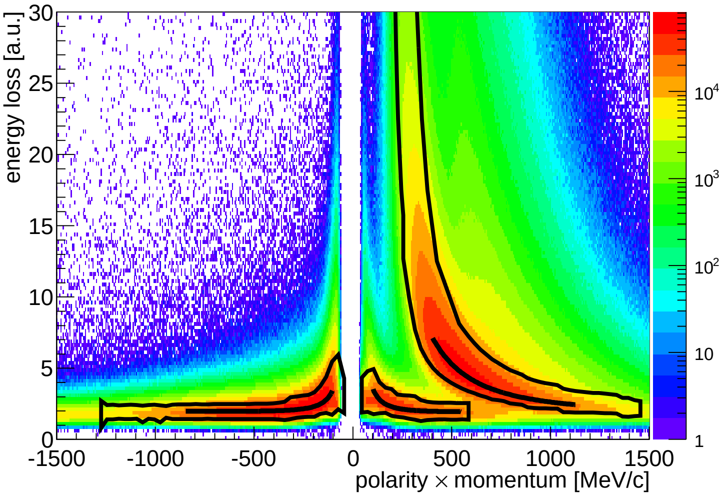

Figure 4.1: Histogram of the energy-loss momentum spectrum. The three bend-like shapes are interpreted as π^-, π^+ and protons (left to right). The black boundaries indicate the graphical cuts, inside of which a track is regarded as an identified particle of the corresponding type.

N_A: Avogadro number

I: mean ionization potential of the material's atoms

δ: density correction

T_max: maximum kinetic energy which can be transferred

The relations $\beta^2\gamma^2 = p^2/m^2$ and $\beta^2 = p^2/(p^2 + m^2)$ from special relativity show that energy loss can not only be seen as a function of speed β, but also of momentum p. However, we then have a dependence on the mass m of the impinging particle.

In fact, we can put graphs of the Bethe-Bloch formula through the structures observed in the $\mathrm{d}E/\mathrm{d}x$ vs. pq spectrum and compare the corresponding m's to known particle masses to associate a particle identification (PID).

The deviation of the measured $\mathrm{d}E/\mathrm{d}x$ from the Bethe-Bloch value, which causes the non-line-like shape of the "particle regions", is due to the statistical nature of energy loss. Bethe and Bloch only give the mean value, but the actual distribution is more complicated. In our analysis, we assume a Landau distribution, which is the theoretical expectation for energy loss in a thin layer [25], smeared with a Gaussian to account for measurement uncertainties [26]. This is achieved with the mathematical operation of convolution ($*$):

$$f(\mathrm{d}E/\mathrm{d}x) \propto \mathrm{Landau}(\mu_\mathrm{L}, \sigma_\mathrm{L}) * \mathrm{Gauss}(0, \sigma_\mathrm{G}) \tag{4.2}$$

To be able to treat the signals of different particle species[1] of the same charge separately, a pre-selection on the literature mass ±100 MeV is performed using the mass information of the META system (cf. Sec. 2.2.5). The corresponding spectra are displayed in Fig. 4.2. By dividing the spectrum into vertical slices (small interval for pq, full range for $\mathrm{d}E/\mathrm{d}x$), several energy loss distributions are obtained and each one is fitted with Eq. 4.2 (see Fig. 4.3 for an example). Each fit yields a width of the distribution, which we define as

$$\bar{\sigma} \equiv \frac{\sigma_\mathrm{L} + \sigma_\mathrm{G}}{2}. \tag{4.3}$$

It is used to define an acceptance $\mu_\mathrm{L} \pm \bar{\sigma}$ interval for that slice. The combination of all successfully fitted intervals for one particle type produces a polygon in the energy loss-momentum plane[2]. All particles inside this cut region are considered as successfully identified representatives of the respective species. Those particles are then assigned their literature mass in order to calculate their full 4-momentum, which is needed for all further analysis steps,

$$p(m, \vec{p}) = \left(\sqrt{m^2 + \vec{p}^2}, \vec{p}\right)^T. \tag{4.4}$$

4.4 Λ Reconstruction

The reconstruction of Λ hyperons is performed using the common *invariant mass method* in combination with *topological cuts*.
As explained in Sec. 3.1, the only Λ decay channel that is experimentally accessible for us is $\Lambda \to p + \pi^-$. Since we do neither know in which events Λs have occurred, nor which protons and pions originate from their decay, we first form every possible combination of a p and a π^- for every event. All of these pairs, called "Λ candidates", are preliminarily treated as if they were physical Λs[3]. The process of Λ reconstruction

---

[1] We will only derive a particle identification for the most abundant hadrons, which are p, π^+ and π^-. Kaons, deuterons etc. remain unidentified, but not unused, cf. Sec. 4.4.1.

[2] However, for protons only the slices for high momenta can be fitted well, because the distribution becomes too broad for low momenta. Instead, the same slicing and fitting procedure is repeated for the horizontal direction, though there is no theoretical justification for using the Landau-Gauss approach on a momentum distribution. The final cut polygon for protons is given by the union of both individual results.

[3] In the following, the index of some quantity Q will indicate its affiliation: $Q_{p\pi}$ belongs to a Λ candidate, whereas Q_Λ describes a physical Λ baryon.

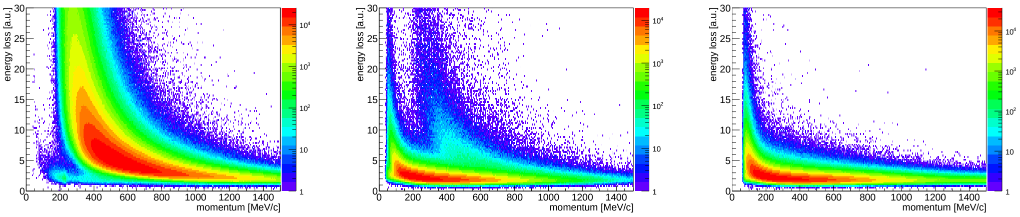

(a) protons (b) positive pions (c) negative pions

Figure 4.2: Energy-loss momentum spectra of the three identified particle species. Each spectrum is filtered by polarity and the corresponding literature mass ±100 MeV using the information of the META system. For protons and π^+ the contamination with particles of same charge is recognizable.

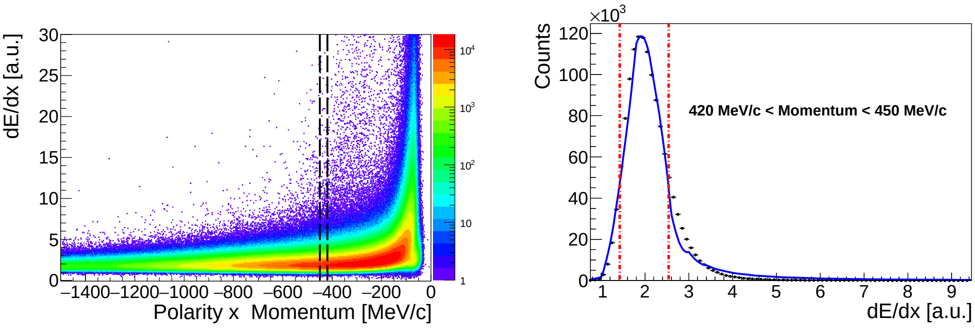

(a) (b)

Figure 4.3: Illustration of the cut finding procedure using the example of π^-. A vertical slice is taken from the energy-loss momentum spectrum (left) and fitted with Eq. 4.2 (right). The red interval yields the range used in the cut. [26]

will gradually eliminate more and more of these candidates, leaving a remainder with an improved fraction of real Λ hyperons. Some contamination with fakes is usually left, but the purity of the sample can be quantified (see Sec. 4.4.1).

With the help of the particle identification method (cf. Sec. 4.3), we can reconstruct the 4-momentum for each Λ candidate from its daughter particles due to energy and momentum conservation:

$$p_{p\pi} = p_p + p_\pi \tag{4.5}$$

Special relativity states that the length of a momentum 4-vector with respect to the Minkowski metric will always be equal to the corresponding particle's mass. Hence, we can calculate an “invariant mass” for all our Λ candidates:

$$m_{p\pi} \equiv \sqrt{p_{p\pi}^2} = \sqrt{E_{p\pi}^2 - \vec{p}_{p\pi}^{\,2}} \tag{4.6}$$

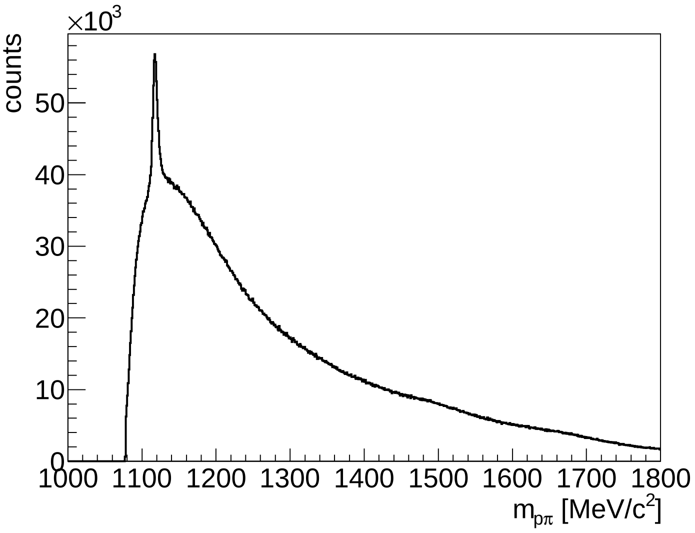

Figure 4.4: Invariant mass spectrum for *all* Λ candidates. It shows a peak around the expected position, which is $m_\Lambda \approx 1116$ MeV.

The lowest possible value for this quantity is the sum of proton and charged pion mass, $m_{p\pi,\mathrm{min}} \approx 1078$ MeV. It is understood that the expectation for actual Λs is $m_{p\pi} \approx m_\Lambda \approx 1116$ MeV (cf. Sec. 3.1). In fact, the experimental invariant mass spectrum given in Fig. 4.4 exhibits a considerable peak at the expected position. However, the majority of the entries appears to be part of a ridge-like shape starting at $m_{p\pi,\mathrm{min}}$ and abating asymptotically to zero for high masses. This is the phenomenon of "combinatorial background", which consists of fake Λ candidates. Since they are not individual particles, but rather mathematical constructs, they can have almost arbitrary "masses".

By fitting the peak and the background with separate functions, we can calculate the number of actual Λ hyperons to about 126000 (see Fig. 4.5). We could already reject a lot of combinatorial background by cutting the spectrum down to some mass interval around m_Λ (mass cut). Still though, with this method alone, we cannot get rid of the background lying directly "underneath" the peak[4]. Therefore, we will first apply more constraints to the Λ candidates, called *topological cuts.*

4.4.1 Topological Cuts

The method of topological cuts takes advantage of the fact that we do not only have kinematic information about the particles, i.e. their 4-momenta, but also know their

---

[4] Although it may appear to the eye, that there is some ordering taking place putting the real Λs "on top" of the background, the data inside the mass cut will remain completely indistinguishable.

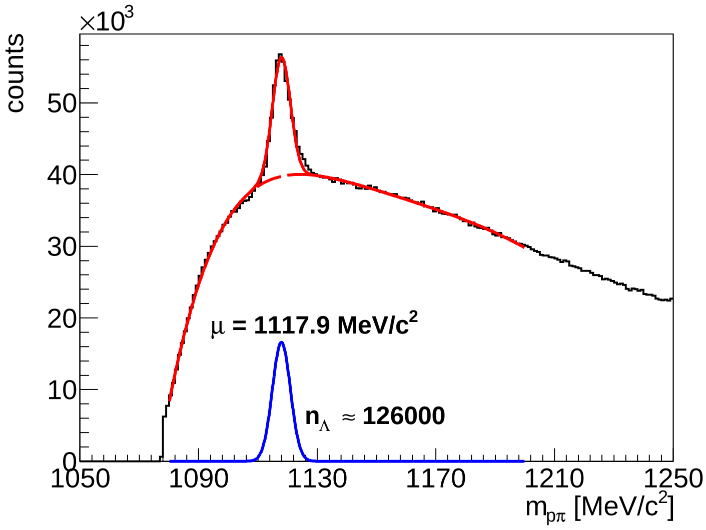

Figure 4.5: Fit of the uncut invariant mass spectrum of Λ candidates. The combinatorial background is modeled as the sum of a Landau function and a polynomial. The peak is fitted with a Gaussian. It is located at 1117.9 MeV and the area underneath gives an estimated number of 126000 Λ hyperons.

spatial paths inside the detector. Tracing back those tracks enables us to tell *where* some process took place, rather than just *how*. Since most particle reactions happen on very small length scales which are far below our spatial detector resolution, we can regard them as punctual. We refer to these points in space as “vertices”.

In theory, the tracks of all particles involved in a reaction should meet in the corresponding vertex. This requirement will not be fulfilled by data recorded with a particle detector because of the finite resolution of its components. Therefore, we need a convention on how to obtain an approximation to the vertex position from the track information.

Although peculiar situations like parallel or intersecting tracks have in general to be taken into account[5], the vast majority of the tracks will be pairwise skew. For two skew straights in three-dimensional space, we can look at the set of line segments that lead from one straight to the other. There will be exactly one segment with minimal length, which we call “distance of closest approach” (DCA). It is perpendicular to both tracks and its midpoint is defined as their “point of closest approach” (PCA). For more than two tracks, the situation is more complicated. In App. A, we

---

[5] It is understood, that for intersecting tracks, the intersection point is chosen as the vertex. For parallel tracks, there is no unique two-particle vertex, so the event is discarded, if there are no additional tracks.

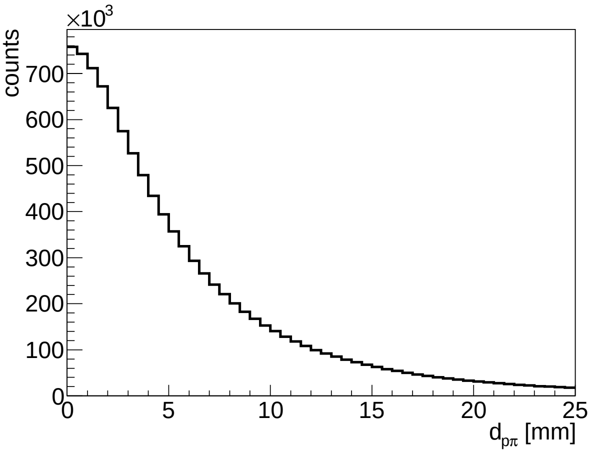

Figure 4.6: Histogram of $d_{p\pi}$ for all Λ candidates. There is no rise towards higher DCAs, because almost all $p\pi^-$ pairs come from a common vertex, be it primary or secondary.

give a suggestion on how to deal with that situation.
We will now describe, how we use the geometrical information to distinguish between actual Λ events and combinatorial background.

Secondary vertex As already mentioned in Sec. 3.1, the Λ decay vertex (secondary vertex) plays an important role in our analysis. For any Λ candidate, it is defined as the PCA of the respective proton and pion track. It is understood that the DCA of the two tracks, in the following denoted as $d_{p\pi}$, is expected to be small for real Λs. Therefore, we will introduce an upper limit cut on it to reduce background.
However, there is no remarkable rise for high $d_{p\pi}$ in the experimental spectrum given in Fig. 4.6, rather the opposite is the case. This is due to the fact that even unrelated $p\pi^-$ pairs usually have a small DCA, because they also come from a common vertex, the primary vertex though.

Primary vertex The primary vertex is the location of the initial pion-nucleus reaction (cf. Sec. 3.2). Thus, we expect all particle tracks[6] except those of Λ daughters to emerge from it. This brings up a whole variety of new cutting possibilities, but first, we have to determine its position.
Although there is some primary vertex estimate provided by the HYDRA framework [23], we decide to recalculate it by ourselves to account for the fact that the

---

[6] This naturally includes the Λs, as well. For each Λ candidate, a track can be defined using its decay vertex as the base and $\vec{p}_{p\pi}$ as the direction.

reconstructed Λ track is supposed to go through it, instead of its proton and pion daughter. To obtain the highest possible precision, we do not only use the tracks of identified particles, but all those which have been accepted by the track sorter (cf. Sec. 4.2). This is possible, because we do *not* need the energy, or mass, respectively, determined in PID to know the track of a particle.
We distinguish three cases:

- For events which have a sole Λ candidate track, i.e. pure $p\pi^-$ events with no other particles present, the vertex should naturally be located on that track. However, there is no other object in this setup to dictate the actual position along the track, but the beam axis. Therefore, we choose the point on the Λ candidate track which is closest to the beam line[7]. This is justified by the fact that we expect collisions to happen, of course, in the beam region.
- If there is one additional track to the Λ candidate, the PCA of those two tracks is chosen.
- For more than two tracks, the procedure described in App. A is applied.

Now that we have a primary and a secondary vertex position, we can impose more topological cuts, which will be explained in the following. Together with the already introduced $d_{p\pi}$ cut, they are shown in Fig. 4.7.
As described in Sec. 3.1, a major characteristic of a certain Λ event is the clear distinguishability of primary and secondary vertex. Hence, we introduce the flight distance l as the length between primary and secondary vertex and set a lower cut threshold to select Λs. The mean distance expected to be covered by a Λ hyperon is

$$\langle s\rangle = v\cdot t = \beta c\cdot\gamma\tau_\Lambda = \beta\gamma\cdot(c\tau_\Lambda) = \frac{|\vec{p}|}{m_\Lambda}\cdot\underbrace{(c\tau_\Lambda)}_{\approx 7.89\text{ cm}}\ . \tag{4.7}$$

Considering the available kinetic energy (cf. Sec. 3.2), the Λ momentum will be around $m_\Lambda/2$, resulting in a range of some centimeters outside of which only about a third of the Λs will be still intact. Hence, the cut on l will indeed improve the chance of a secondary vertex to be a Λ decay vertex, but it will also discard a significant amount of Λs.
As already mentioned, we expect the Λ track to go through both the secondary and the primary vertex. A weaker form of this condition is the requirement on $\vec{p}_{p\pi}$ to be parallel to the vector pointing from one vertex to the other. This brings up the angle α between the two vectors, which should be small (ideally 0°).
It was noted in the context of $d_{p\pi}$ that mistaking particles from the primary vertex

---

[7] This is *not* a point of closest approach in the sense of the above definition. It is not located in between the straights, but *on* one of them.

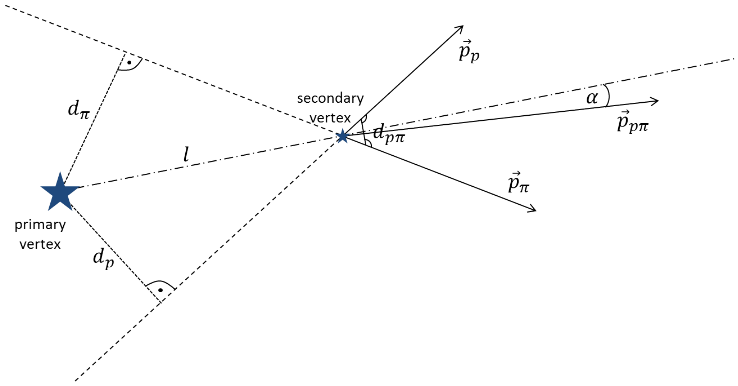

Figure 4.7: Illustration of the topological cuts used in our analysis.
$d_{p\pi}$ is the distance of closest approach between proton and pion track. The distance of primary and secondary vertex is indicated by l. The angle α is measured between the connection line of the vertices and the Λ candidate momentum $\vec{p}_{p\pi} = \vec{p}_p + \vec{p}_\pi$. d_p and d_π are the distances of closest approach of proton and pion to the primary vertex.

for Λ daughters will cause problems. Another pair of cut parameters of which it is understood that they sacrifice statistic to improve purity, are thus the distances of closest approach of the proton (d_p) and pion track (d_π) towards the primary vertex. Imposing a lower threshold on them will in turn improve the functioning of $d_{p\pi}$.

Selecting a topological cut combination The listing above already introduced the problem of contrariness between the cardinality and purity of a Λ sample achieved with topological cuts. It is therefore a major task to find an optimal set of thresholds to produce an acceptable amount of Λs for a further analysis while providing the necessary low contamination with fakes.
Since it is in general not easy to predict the effect of some cut threshold and the individual cuts may even influence each other, an empirical grid search is performed over the 5-dimensional space of possible threshold values T_i. To be able to compare points on the grid (i.e. cut combinations), we need to establish some measure on them. This is achieved by fitting[8] both the peak and the background in the mass spectrum obtained from applying the respective cuts. Some examples for such cut spectra are given in Fig. 4.8. The integral of the fit functions over $\mu \pm 2\sigma$ represents the number of Λs (“signal”, s) and fake Λ candidates (“background”, b) inside this interval. The optimal combination of cut thresholds should provide both a high s

---

[8] As fit function, we choose a 4-th order polynomial background and two added Gaussian distributions for the peak. The mean μ and the width σ of the total peak are calculated as the amplitude-weighted averages of both individual Gaussians.

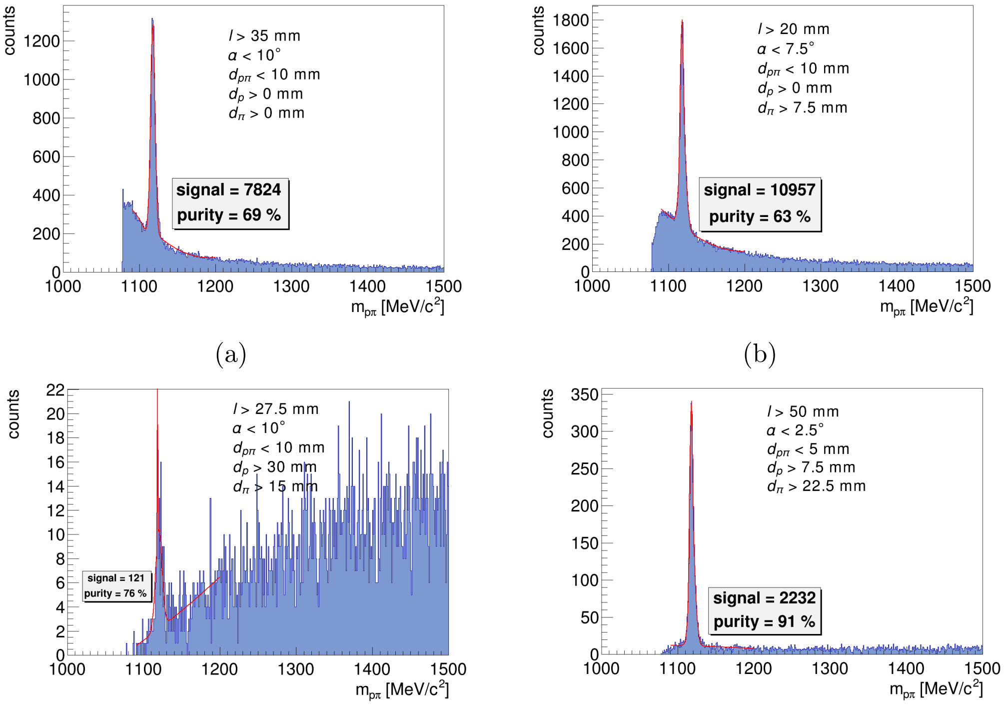

(a) (b)

(c) (d)

Figure 4.8: Invariant mass spectra obtained from applying random combinations of topological cut threshold on the set of Λ candidates. The trade-off between signal (number of Λ hyperons) and sample purity is manifest. Spectrum 4.8c demonstrates the worsening of the fit for histograms with few entries.

and a high purity $s/(s+b)$, which is the fraction of the selected set of Λ candidates that is considered to be real Λ hyperons.

We choose to test the range given in Tab. 4.2 with a $(5 \times 5 \times 5 \times 5 \times 5)$ grid (five thresholds with five increments, each), which thus has 3125 points. Each cut combination is labeled with a 5-digit quinary (base-5) number, where every place stands for one cut parameter and the digit in that place (0 to 4) for the increment inside the tested range. However, we will usually use the decimal equivalent of this number to address the combinations.

In Fig. 4.9, signal and purity for all cut combinations are displayed. The most favorable one is chosen from Fig. 4.10, where the results of the grid analysis are shown in the signal-purity plane. As we would like to have a purity around 90% or better, we choose cut combination 1943, which gives the highest signal for this range. Retranslating it into a combination of cut thresholds yields Tab. 4.3.

threshold for	loosest option	strictest option
l	20 mm	50 mm
α	10°	0°
$d_{p\pi}$	20 mm	0 mm
d_p	0 mm	30 mm
d_π	0 mm	30 mm

Table 4.2: Region of the 5-dimensional space of possible cut thresholds over which the grid search is performed. Each threshold is varied from the loosest option (0th increment) in discrete steps until the strictest option.

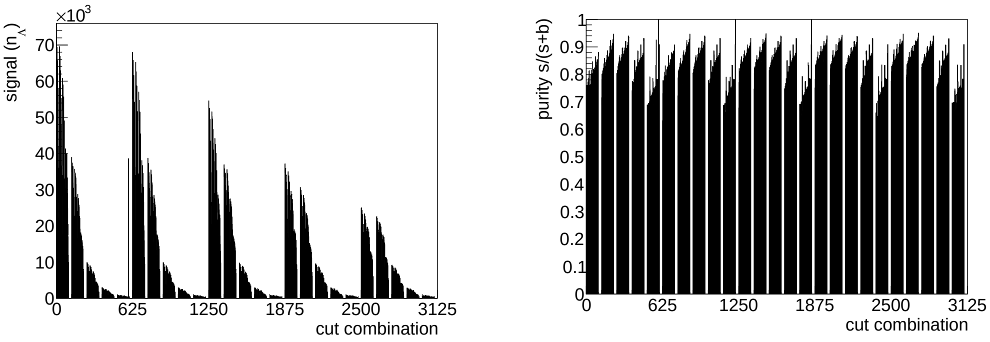

(a)

(b)

Figure 4.9: Analysis of different cut combinations. Each bin on the "cut combination" axis refers to one set of cut thresholds in the domain given in Tab. 4.2. There is a remarkable signal reduction for stricter cuts (left). The purity is quite high for most cuts in the tested range, because even the loosest cut is already effective (right). The sudden one-bin peaks originate from failed mass spectrum fits.

cut parameter	direction	threshold
l	$>$	42.5 mm
α	$<$	2.5°
$d_{p\pi}$	$<$	10 mm
d_p	$>$	0 mm
d_π	$>$	22.5 mm

Table 4.3: The combination of topological cut thresholds which is chosen for our analysis (cut combination 1943).

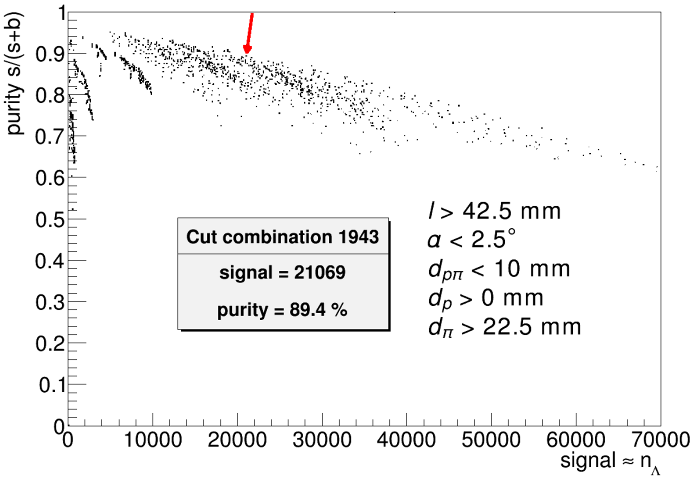

Figure 4.10: Purity $s/(s+b)$ is plotted against signal strength s for 3125 different combinations of topological cut thresholds. For a required purity level of $\sim 90\%$, the cut with the highest signal ($\approx$ number of Λs) is chosen, which is 1943 (red arrow).

The mass spectrum obtained from applying these cuts is given in Fig. 4.11. The fit points out a Λ purity of 89.4% for this sample. With an estimated number of 21069 real Λs, we have a cut efficiency of about 16.7%. Additionally, we obtain as mass cut interval 1112.4 MeV $\leq m_{p\pi} \leq$ 1125.0 MeV.

4.5 The Kinematic Refit

The kinematic refit is a mathematical tool which is commonly used in the context of exclusive analyses of particle reactions. It modifies the measured data in a mathematically and physically justified way, aiming for an improvement of the resolution of certain quantities, e.g. masses of reconstructed particles.

Theory imposes several general constraints upon particle tracks emerging from an elementary process. For instance, tracks of daughter particles from a common mother should intersect at some decay vertex (vertex constraint) and the mass of a reconstructed particle (e.g. via the invariant or missing mass technique) ought to be equal to a given literature value (mass constraint). Furthermore, there should be a global conservation of energy and momentum (conservation constraint).

However, these requirements will hardly be met by experimentally collected data due to issues like the finite resolution of detector components and random technical failures. The mathematical procedure of the refit takes advantage of these statistical uncertainties by shifting the corresponding quantities within that range, trying

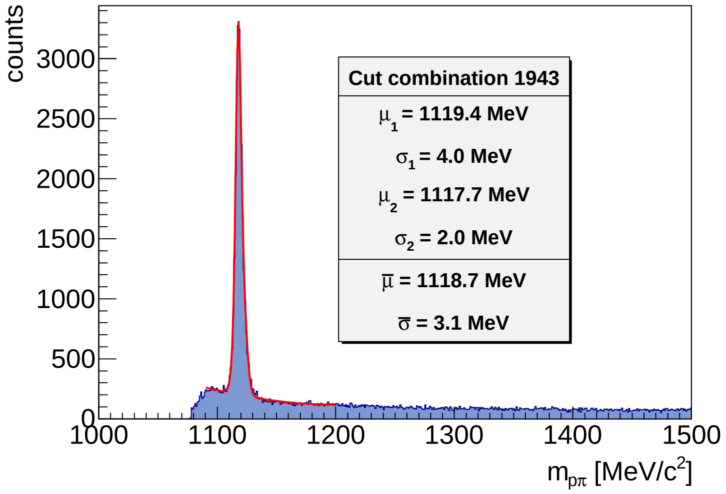

Figure 4.11: Final Λ candidate mass spectrum after applying the optimized cuts (cut combination 1943). A double Gaussian fit of the peak provides a mass cut interval of 1112.4 MeV $\leq m_{p\pi} \leq$ 1125.0 MeV.

to make the data match the theoretical constraints. Accordingly, some knowledge about the technical specifications of the used detector is obligatory (cf. Sec. **??**). The application of the kinematic refit to an *inclusive* analysis is rather exotic due to its sensibility to combinatorial background, since such events are not subject to the physical constraints the whole procedure is based on. However, in our analysis we use this particular "problem" to distinguish between physical events and background (see Sec. 4.5.4 and Ch. 5).

4.5.1 Track Representations

The track of a free point particle is fully defined by its 4-momentum $p = (E, \vec{p})^T$ and the so-called "emission point", some point $\vec{r}$ in space that is crossed by the particle (e.g. a detector hit). If an adequate time resolution was available, the emission point could be extended to be a 4-vector as well, but since that is not the case for our analysis, this option will not be further discussed in the following. For identified particles the mass m is known (see. Sec. 4.3), so the energy E is not needed, but can be calculated from the 3-momentum $\vec{p}$ via the relativistic energy momentum relation

$$E(\vec{p}) = \sqrt{m^2 + \vec{p}^2}. \tag{4.8}$$

Hence, we have reduced the amount of data needed to describe one track to two 3-vectors $\vec{p}$ and $\vec{r}$, yielding 6 parameters. We combine these parameters to one six-dimensional vector $\vec{\alpha}$.

The way to express $\vec{\alpha}$ is not mathematically unique, but we can chose different representations, i.e. coordinate systems. One possibility is the use of pure Cartesian coordinates $\vec{\alpha} = (p_x, p_y, p_z, x, y, z)^T$, but in this analysis, we will use a combination of modified spherical and Cartesian coordinates $\vec{\alpha} = (1/|\vec{p}|, \theta_{\vec{p}}, \varphi_{\vec{p}}, x, y, z)^T$. This accounts for the fact that HADES measures the initial direction of a particle as polar and azimuthal angle, but the magnitude of the momentum is determined by the *curvature* of the track in the magnetic field, which is proportional to $1/|\vec{p}|$ (cf. Sec. 2.2.4).

In general, as soon as we are dealing with one specific experiment, we need to use the appropriate representation for the detector in use. It is imposed by the functionality of the refit: As already mentioned, the crux is to shift the quantities that are *actually measured* within their measurement uncertainties. Thus, it is those quantities which should constitute $\vec{\alpha}$.

4.5.2 Mathematical Considerations

The goal of the kinematic refit is to make the particle tracks of an event fulfill the constraints "as good as possible" while keeping the deviation from the original data within given errors. This problem is known in mathematics as *constrained optimization* and its solution can usually be achieved by the well-known method of Lagrange multipliers.

However, we first need mathematical concepts to describe our constraints and the shift of the data. The m conditions for the tracks are defined in a holonomic way

$$\vec{H}(\vec{\alpha}) = 0, \tag{4.9}$$

where $\vec{H}$ is a m-dimensional vector of equations and $\vec{\alpha}$ now and in the following denotes not only the 6 parameters of one track, but the $6n$ parameters of all n tracks that take part in the reaction. The deviation of $\vec{\alpha}$ from the original measurements $\vec{\alpha}_0$ is expressed by the well-known χ^2 value:

$$\chi^2(\vec{\alpha}) = (\vec{\alpha} - \vec{\alpha}_0)^T \boldsymbol{V}_{\vec{\alpha}_0}^{-1} (\vec{\alpha} - \vec{\alpha}_0) = \sum_{i=1}^{6n} \frac{(\alpha_i - \alpha_{0,i})^2}{\sigma_{\alpha_i}^2} \tag{4.10}$$

$\boldsymbol{V}_{\vec{\alpha}_0}$ is the $6n \times 6n$ covariance matrix containing the variances $\sigma_{\alpha_i}^2$ of the originally measured track parameters. It is important to mention that the random errors of the measurements have implicitly assumed to be Gaussian distributed by introducing χ^2, but this is usually a good approximation (cf. [27]). If the measurements are uncorrelated (as they are supposed to be), the covariance matrix is diagonal and its inverse is

$$\boldsymbol{V}_{\vec{\alpha}_0}^{-1} = \begin{pmatrix} \frac{1}{\sigma_{\alpha_1}^2} & 0 & \cdots & 0 \\ 0 & \frac{1}{\sigma_{\alpha_2}^2} & \cdots & 0 \\ \vdots & \vdots & \ddots & \vdots \\ 0 & 0 & \cdots & \frac{1}{\sigma_{\alpha_{6n}}^2} \end{pmatrix}, \tag{4.11}$$

leading to the last expression in Eq. 4.10.

The method of Lagrange multipliers To minimize $\chi^2(\vec{\alpha})$ while keeping $\vec{H}(\vec{\alpha}) = 0$ valid, the method of Lagrange multipliers defines the Lagrangian

$$L(\vec{\alpha}, \vec{\lambda}) = \chi^2(\vec{\alpha}) + 2\vec{\lambda}^T \vec{H}(\vec{\alpha}) = (\vec{\alpha} - \vec{\alpha}_0)^T \boldsymbol{V}_{\vec{\alpha}_0}^{-1} (\vec{\alpha} - \vec{\alpha}_0) + 2\vec{\lambda}^T \vec{H}(\vec{\alpha}). \tag{4.12}$$

It introduces the m-dimensional vector $2\vec{\lambda}$ containing the eponymous Lagrange multipliers. The reason why the factor 2 is separate and not included into the symbol $\vec{\lambda}$ will become clearer in the following, where it will simplify calculations.
We know replace the minimization of χ^2 with respect to $\vec{\alpha}$ by the minimization of L with respect to both $\vec{\alpha}$ *and* $\vec{\lambda}$. This features the necessary conditions

$$0 \overset{!}{=} \vec{\nabla}_{\vec{\alpha}} L \qquad = \vec{\nabla}_{\vec{\alpha}} \chi^2(\vec{\alpha}) + 2 \sum_{i=1}^{m} \lambda_i \vec{\nabla}_{\vec{\alpha}} H_i(\vec{\alpha}), \tag{4.13}$$

$$0 \overset{!}{=} \frac{1}{2} \vec{\nabla}_{\vec{\lambda}} L \qquad = \vec{H}(\vec{\alpha}). \tag{4.14}$$

The second condition obviously ensures compliance with the constraints. The first condition demands a linear dependence of the gradient of $\chi^2(\vec{\alpha})$ on the gradients of the m constraint equations.
The effect of this request can be explained best in a model scenario with only two parameters α_1 and α_2 and one constraint equation $H(\alpha_1, \alpha_2) = 0$. Here, χ^2 and H are scalar functions in a two-dimensional α_1-α_2-plane and can thus be visualized by a contour plot (see Fig. **??**). An important role is held by the contour $H(\alpha_1, \alpha_2) = 0$, because this is where the desired physical solutions live. Eq. 4.13 now reads

$$\vec{\nabla}_{\alpha_1,\alpha_2} \chi^2(\alpha_1, \alpha_2) = -2\lambda \vec{\nabla}_{\alpha_1,\alpha_2} H(\alpha_1, \alpha_2), \tag{4.15}$$

telling us that the gradients of χ^2 and H should be collinear. Since the gradient of a smooth function is always perpendicular to its contour lines, this means we are looking for a contour of χ^2 that is tangential to $H = 0$. It belongs to some value $\chi^2(\alpha_1, \alpha_2) = \chi^2_{\text{min}}$ at which $\chi^2(\vec{\alpha})\big|_{\vec{H}(\vec{\alpha})=0}$ is stationary[9]. The location $\vec{\alpha}_{\text{opt.}} = (\alpha_1, \alpha_2)^T$ of the osculation point is the desired result of the refit procedure.

---

[9] The discussion, whether this stationary point is actually a minimum or a maximum goes beyond our scope and can be looked up in mathematical literature. In our analysis, we assume it to be a *local minimum*, which is be justified by the success of the procedure.

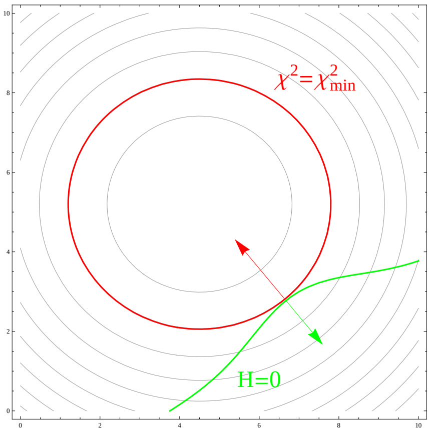

Figure 4.12: Illustration of the method of Lagrange multipliers in a 2-dimensional scenario. The contour $\chi^2 = \chi^2_{\text{min}}$, which is tangent to $H = 0$, belongs to the minimal χ^2 value that can be reached under these constraints.

In the context of an experimental analysis, it is though important to mention that the solution $\vec{\alpha}$ of the Lagrangian method does not necessarily yield the actual tracks $\vec{\alpha}_{\text{real}}$ in the physical event. It is merely the candidate for a physical track configuration which is (in the sense of χ^2) "closest" to the measurements $\vec{\alpha}_0$. This situation is depicted in Fig. 4.13. However, it is assumed that the refitted $\vec{\alpha}$ is closer to $\vec{\alpha}_{\text{real}}$ than $\vec{\alpha}_0$ used to be and that this leads to a better final result.

Implementation of the kinematic refit procedure In the following, we will describe how we actually implement the mathematical considerations given above in our analysis. This realization is mainly based on the work of Paul Avery [28] and has proven to be successful in exclusive analyses (cf. [29], [27]).
The conditions

$$\begin{aligned} 0 &\overset{!}{=} \frac{\partial L}{\partial \vec{\alpha}} = 2(\vec{\alpha} - \vec{\alpha}_0)^T \boldsymbol{V}^{-1}_{\vec{\alpha}_0} + 2\vec{\lambda}^T \frac{\partial \vec{H}(\vec{\alpha})}{\partial \vec{\alpha}}, \\ 0 &\overset{!}{=} \frac{\partial L}{\partial \vec{\lambda}} = 2\vec{H}^T(\vec{\alpha}). \end{aligned} \tag{4.16}$$

(now written in matrix notation with the Jacobian $\frac{\partial \vec{H}(\vec{\alpha})}{\partial \vec{\alpha}}$) can be highly non linear in $\vec{\alpha}$, making it impossible to solve this system of equations analytically.
Instead, we replace the direct solution by an iterative procedure with linearized constraint equations. We will now look for the solution $\vec{\alpha}_{k+1}$ of the next step $k+1$, assuming $\vec{\alpha}_k$ for the current step k is given. To get rid of the nonlinearity, we expand our constraint equations to first order around a point which is close to $\vec{\alpha}_{k+1}$.

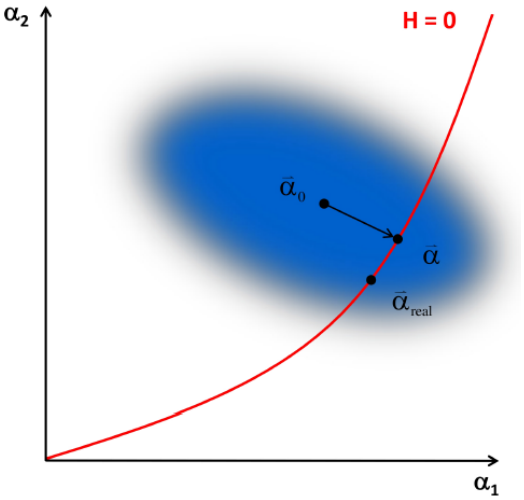

Figure 4.13: The refit result $\vec{\alpha}$ does not necessarily equal the real track configuration $\vec{\alpha}_{\text{real}}$. However, it is usually closer to it than the original measurement $\vec{\alpha}_0$. The blue ellipse indicates the uncertainty range of $\vec{\alpha}_0$.

Assuming that one iteration step changes the data only little, the best candidate for that is obviously the solution of the current step, $\vec{\alpha}_k$. Thus, we choose the expansion of $\vec{H}(\vec{\alpha}_{k+1})$ around $\vec{\alpha}_k$:

$$\vec{H}(\vec{\alpha}_{k+1}) = \vec{H}(\vec{\alpha}_k) + \left.\frac{\partial \vec{H}(\vec{\alpha})}{\partial \vec{\alpha}}\right|_{\vec{\alpha}=\vec{\alpha}_k} (\vec{\alpha}_{k+1} - \vec{\alpha}_k) + \mathcal{O}\left(|\vec{\alpha}_{k+1} - \vec{\alpha}_k|^2\right) \tag{4.17}$$

With the notations $\boldsymbol{D}_k \equiv \left.\frac{\partial \vec{H}(\vec{\alpha})}{\partial \vec{\alpha}}\right|_{\vec{\alpha}=\vec{\alpha}_k}$ and $\vec{d}_k \equiv \vec{H}(\vec{\alpha}_k)$, our linearized Lagrangian now reads

$$\begin{aligned} &L(\vec{\alpha}_{k+1}, \vec{\lambda}_{k+1}) \\ &= (\vec{\alpha}_{k+1} - \vec{\alpha}_0)^T \boldsymbol{V}_{\vec{\alpha}_0}^{-1} (\vec{\alpha}_{k+1} - \vec{\alpha}_0) + 2\vec{\lambda}_{k+1}^T (\boldsymbol{D}_k (\vec{\alpha}_{k+1} - \vec{\alpha}_k) + \vec{d}_k), \end{aligned} \tag{4.18}$$

with the minimization conditions

$$\begin{aligned} 0 &\overset{!}{=} \frac{\partial L}{\partial \vec{\alpha}_{k+1}} = 2(\vec{\alpha}_{k+1} - \vec{\alpha}_0)^T \boldsymbol{V}_{\vec{\alpha}_0}^{-1} + 2\vec{\lambda}_{k+1}^T \boldsymbol{D}_k, \\ 0 &\overset{!}{=} \frac{\partial L}{\partial \vec{\lambda}_{k+1}} = 2(\boldsymbol{D}_k (\vec{\alpha}_{k+1} - \vec{\alpha}_k) + \vec{d}_k)^T. \end{aligned} \tag{4.19}$$

This leads to an equation system which is now solvable:

$$\begin{aligned} \boldsymbol{V}_{\vec{\alpha}_0}^{-1} (\vec{\alpha}_{k+1} - \vec{\alpha}_0) + \boldsymbol{D}_k^T \vec{\lambda}_{k+1} &= 0, \\ \boldsymbol{D}_k (\vec{\alpha}_{k+1} - \vec{\alpha}_k) + \vec{d}_k &= 0. \end{aligned} \tag{4.20}$$

It is easy to see the dependence of $\vec{\alpha}_{k+1}$ on $\vec{\lambda}_{k+1}$

$$\vec{\alpha}_{k+1} = \vec{\alpha}_0 - \boldsymbol{V}_{\vec{\alpha}_0} \boldsymbol{D}_k^T \vec{\lambda}_{k+1}, \tag{4.21}$$

but the solution for $\vec{\lambda}_{k+1}$ is a little more complicated to obtain. It emerges that the matrix product $\boldsymbol{D}_k \boldsymbol{V}_{\vec{\alpha}_0} \boldsymbol{D}_k^T$ has to be inverted. Since $\boldsymbol{V}_{\vec{\alpha}_0}$ has only non-zero diagonal entries, the desired invertibility depends only on the question, whether $\boldsymbol{D}_k$ has full row rank. This is satisfied, if there are as many or more track parameters than constraints, i.e. $n \geq m$, and there are no redundant constraints. The inverse is then called

$$\boldsymbol{V}_D \equiv (\boldsymbol{D}_k \boldsymbol{V}_{\vec{\alpha}_0} \boldsymbol{D}_k^T)^{-1}. \tag{4.22}$$

It is reasonable to mention that $\boldsymbol{V}_D$ is symmetric.
We can now write the solution for $\vec{\lambda}_{k+1}$ as

$$\vec{\lambda}_{k+1} = \boldsymbol{V}_D(\boldsymbol{D}_k(\vec{\alpha}_0 - \vec{\alpha}_k) + \vec{d}_k). \tag{4.23}$$

By inserting this into Eq. 4.21, we can also obtain the solution for $\vec{\alpha}_{k+1}$:

$$\vec{\alpha}_{k+1} = \vec{\alpha}_0 - \boldsymbol{V}_{\vec{\alpha}_0} \boldsymbol{D}_k^T \boldsymbol{V}_D(\boldsymbol{D}_k(\vec{\alpha}_0 - \vec{\alpha}_k) + \vec{d}_k) \tag{4.24}$$

However, we are not only interested in the refitted data $\vec{\alpha}_{k+1}$, but also in its covariance matrix $\boldsymbol{V}_{\vec{\alpha}_{k+1}}$ to investigate the change of the uncertainties caused by the refit. The vector $\Delta\vec{\alpha}_{k+1}$ of uncertainties is obtained by standard Gaussian error propagation from the original uncertainties $\Delta\vec{\alpha}_0$:

$$\Delta\vec{\alpha}_{k+1} = \frac{\partial \vec{\alpha}_{k+1}}{\partial \vec{\alpha}_0} \Delta\vec{\alpha}_0 = (\mathbb{1} - \boldsymbol{V}_{\vec{\alpha}_0} \boldsymbol{D}_k^T \boldsymbol{V}_D \boldsymbol{D}_k)\Delta\vec{\alpha}_0 \tag{4.25}$$

This yields a covariance matrix

$$\boldsymbol{V}_{\vec{\alpha}_{k+1}} = \Delta\vec{\alpha}_{k+1}(\Delta\vec{\alpha}_{k+1})^T = \boldsymbol{V}_{\vec{\alpha}_0} - \boldsymbol{V}_{\vec{\alpha}_0} \boldsymbol{D}_k^T \boldsymbol{V}_D \boldsymbol{D}_k \boldsymbol{V}_{\vec{\alpha}_0}. \tag{4.26}$$

It can be shown that the expression following the minus sign is always a diagonal matrix with positive entries. Thus, the refit always causes the variances to decrease, which is consistent with the assumption that the refitted track configuration is closer to the actual physical one. This fact will also play an important role in the next section.
Another quantity of interest is the χ^2 value of the refitted data. Using Eq. 4.24, it calculates to

$$\begin{aligned} \chi^2_{k+1} &= (\vec{\alpha}_{k+1} - \vec{\alpha}_0)^T \boldsymbol{V}_{\vec{\alpha}_0}^{-1} (\vec{\alpha}_{k+1} - \vec{\alpha}_0) \\ &= \left(\boldsymbol{D}_k(\vec{\alpha}_0 - \vec{\alpha}_k) + \vec{d}_k\right)^T \boldsymbol{V}_D \left(\boldsymbol{D}_k(\vec{\alpha}_0 - \vec{\alpha}_k) + \vec{d}_k\right). \end{aligned} \tag{4.27}$$

Since $\boldsymbol{V}_D$ is an $m \times m$ matrix, the number of degrees of freedom (NDF) of the refit equals the number of constraint equations[10]. This information will be needed when discussing the quality of the refit.

Conclusion We have know developed an iterative approach to the concept of the kinematic refit. With Eq.'s 4.24, 4.26 and 4.27, one can calculate an arbitrary number of iteration steps, starting from the original data $k = 0$. The result of one step is used as the input for the next step ($k \to k+1$). This procedure will converge on some track configuration, which is then regarded as the result. Since the constraints $\vec{H}(\vec{\alpha})$ usually vary slowly as functions of $\vec{\alpha}$, only few iterations are needed ([29],[27]). In our analysis, we use 10 iteration steps, if nothing else is mentioned.

4.5.3 Applicability to the $\pi^- W$ analysis

In order to apply the kinematic refit to a specific analysis, we first need to take a look at the possible holonomic constraints for the corresponding experimental setup. This reveals a general problem in the context of inclusive analyses.
Because we can neither access the exact properties of the initial particles, nor be sure to have detected all final particles, nor even know in detail what happened during the reaction, many of the constraints we have mentioned in the introduction about the refit (cf. Sec. 4.5) cannot be checked for validity. This means, we are not able to calculate the corresponding $H_i(\vec{\alpha})$, because $\vec{\alpha}$ contains quantities which are not available to our analysis. In particular, we cannot use conservation constraints and have limited possibilities concerning vertex constraints.
In fact, the only quantities we have mentioned so far which are supposed to equal one specific value[11] are $m_{p\pi} \overset{!}{=} m_\Lambda$, $d_{p\pi} \overset{!}{=} 0$ mm and $\alpha \overset{!}{=} 0°$. In the following, we will discuss a kinematic refit on these values, which arise in the context of Λ reconstruction.

Finding holonomic constraint equations The first step in implementing the refit for a concrete set of constraints is formulating the holonomic constraint equations $\vec{H}(\vec{\alpha}) = 0$.
As it was already explained in Sec. 4.5.1, we use the $\vec{\alpha} = (1/|\vec{p}|, \theta_{\vec{p}}, \varphi_{\vec{p}}, x, y, z)^T$ track representation, when working with HADES data. Thus, it is comparably easy to work with geometrical tracks, since they only depend on the vertex position and the angles $\theta_{\vec{p}}$ and $\varphi_{\vec{p}}$, but not on the momentum magnitude. However, for kinematic

---

[10] Avery also discusses the introduction of unknown parameters, e.g. for vertex constraints of more than two tracks. These parameters reduce the NDF. However, this extension to the refit procedure is not be used in our analysis.

[11] In contrast to quantities which have continuous behavior, like l, d_p or d_π.

track parameter	uncertainty	track parameter	uncertainty
$1/\|\vec{p}_p\|$	3.5%	$1/\|\vec{p}_\pi\|$	4.1%
$\theta_{\vec{p}_p}$	0.55%	$\theta_{\vec{p}_\pi}$	1.2%
$\varphi_{\vec{p}_p}$	1.4%	$\varphi_{\vec{p}_\pi}$	7.6%
x_p	20 mm	x_π	20 mm
y_p	20 mm	y_π	20 mm
z_p	20 mm	z_π	20 mm

Table 4.4: Table of the uncertainties used for kinematic refits on HADES data. Percentages indicate relative uncertainties. [27]

constraints, we still need $1/|\vec{p}|$. The uncertainties of the track parameters were already analyzed for HADES and are taken from [27]. They are listed in Tab. 4.4. Apparently, the constraints mentioned above can equivalently be formulated as

$$H_1(\vec{\alpha}) = m_\Lambda^2 - m_{p\pi}^2 = 0, \tag{4.28}$$

$$H_2(\vec{\alpha}) = d_{p\pi} = 0, \tag{4.29}$$

$$H_3(\vec{\alpha}) = \cos(\alpha) - 1 = 0. \tag{4.30}$$

We will now work out the dependence of these holonomic constraints on the track parameters $\vec{\alpha}$, which comprise the proton and pion daughter tracks of the refitted Λ candidate. Though, we will not derive the partial derivatives needed for the refit in explicit, as they are quite lengthy. They can be easily obtained using a computer algebra system.

The first constraint H_1 can be expressed through the 3-momenta using special relativity and the definition of the invariant mass:

$$\begin{aligned} H_1(\vec{p_p}, \vec{p_\pi}) &= m_\Lambda^2 - (m_p^2 + m_\pi^2 + 2p_p \cdot p_\pi) \\ &= m_\Lambda^2 - m_p^2 - m_\pi^2 + 2\vec{p}_p \cdot \vec{p}_\pi - 2\sqrt{\vec{p}_p^2 + m_p^2}\sqrt{\vec{p}_\pi^2 + m_\pi^2} \end{aligned} \tag{4.31}$$

The second constraint H_2 is purely geometric, so we use the unit momenta

$$\hat{p} \equiv \frac{\vec{p}}{|\vec{p}|} = (\sin\theta\cos\varphi, \sin\theta\sin\varphi, \cos\theta)^T \tag{4.32}$$

and the vertex positions $\vec{r} = (x, y, z)^T$. The DCA of the tracks is then given by the magnitude of the component of $\vec{r}_p - \vec{r}_\pi$ which is perpendicular to both tracks. Considering the mathematical properties of the dot and the cross product, this can be written as

$$H_2(\hat{p}_p, \vec{r}_p, \hat{p}_\pi, \vec{r}_\pi) = (\vec{r}_p - \vec{r}_\pi) \cdot \frac{\hat{p}_p \times \hat{p}_\pi}{|\hat{p}_p \times \hat{p}_\pi|}. \tag{4.33}$$

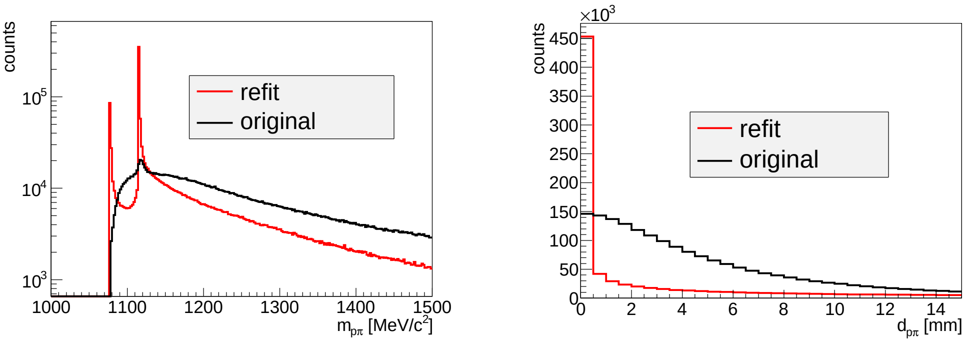

(a) $m_{p\pi}$ (b) $d_{p\pi}$

Figure 4.14: Effect of the refit to the constraints H_1 and H_2 on the corresponding quantities $m_{p\pi}$ (left) and $d_{p\pi}$ (right). The mass converges mostly (log scale!) on the expected m_Λ, but some Λ candidates get stuck on $m_p + m_\pi$.

The third constraint H_3 does not only depend on the proton and pion tracks, but also on the primary vertex position $\vec{r}_\mathrm{I}$. We regard this point as immovable, i.e. it will not be changed through the refit. It is thus not part of $\vec{\alpha}$, but has to be treated separately.

The secondary vertex $\vec{r}_\mathrm{II}$, which is the PCA of proton and pion, can be expressed as an extensive function of $\vec{\alpha}$. With this function, we can write

$$H_3(\vec{\alpha}, \vec{r}_\mathrm{I}) = \frac{(\vec{r}_\mathrm{II}(\vec{\alpha}) - \vec{r}_\mathrm{I}) \cdot (\vec{p}_p + \vec{p}_\pi)}{|\vec{r}_\mathrm{II}(\vec{\alpha}) - \vec{r}_\mathrm{I}||\vec{p}_p + \vec{p}_\pi|} - 1 \tag{4.34}$$

Apparently, the partial derivatives of this expression are extremely extensive, which makes them unfeasible for any analytic handling of this constraint. A numerical approach may succeed, but this goes beyond the scope of this work. In Ch. 6, we will point out another option to be worked on in the future.

As a consequence, there are now only two appropriate constraints left for the kinematic refit of the Λ candidates. The effect of this refit on the corresponding quantities $m_{p\pi}$ and $d_{p\pi}$ is displayed in Fig. 4.14.

4.5.4 Analysis of Refit Results

In Sec. 4.5, we already suggested that the kinematic refit is very sensitive to combinatorial background. If we try to refit a fake Λ candidate, its track parameters $\vec{\alpha}$ usually have to be shifted quite far (compared to the uncertainty ranges). This results in a large χ^2 value of the refit according to Eq. 4.10. Thus, we can use a large χ^2 as an indicator for combinatorial background.

If all uncertainties are Gaussian distributed and estimated correctly, the χ^2 value

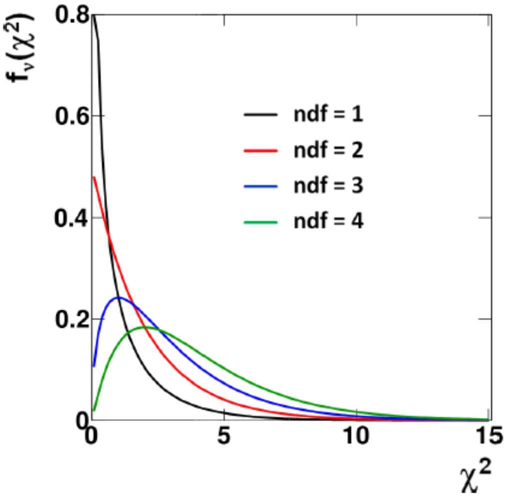

Figure 4.15: Plots of the χ^2 distribution for different numbers of degrees of freedom (ndf). For higher ndf, the distribution shifts to the right to maintain a mean value equal to ndf. This corresponds to the expectation that more shifting of $\vec{\alpha}$ has to be done, if there are more constraint equations. [29]

follows the χ^2 distribution with the density function

$$f_\nu(\chi^2) = \frac{1}{2^{\nu/2}\Gamma(\nu/2)}(\chi^2)^{\nu/2-1}\mathrm{e}^{-\frac{1}{2}\chi^2}, \tag{4.35}$$

where Γ is the gamma function. The integer parameter ν is both the number of degrees of freedom (ndf) and the mean value of the distribution $\langle\chi^2\rangle = \nu$. The appropriate ndf for our analysis is given by the number of constraint equations of the refit (which is either 1 or 2, see below).

As the shape of the χ^2 distribution strongly depends on ν (see Fig. 4.15 for example plots), it is convenient to define another quantity, the so-called "p-value":

$$\text{p-value}(\chi^2) \equiv \int_{\chi^2}^{\infty} f_\nu(\tilde{\chi}^2)\mathrm{d}\tilde{\chi}^2 \tag{4.36}$$

It indicates the probability for a fit with a certain χ^2 that there will be another fit which is "worse" (i.e. has a higher χ^2). Its advantage over χ^2 is the fact that it is always between 0 and 1 because of the normalization of $f_\nu(\chi^2)$. Furthermore, it is supposed to be evenly distributed inside this range, if the input to the fit is valid (i.e. there is no background) and all uncertainties are estimated correctly. [27]

However, since we inevitably *do* have combinatorial background in our data, the

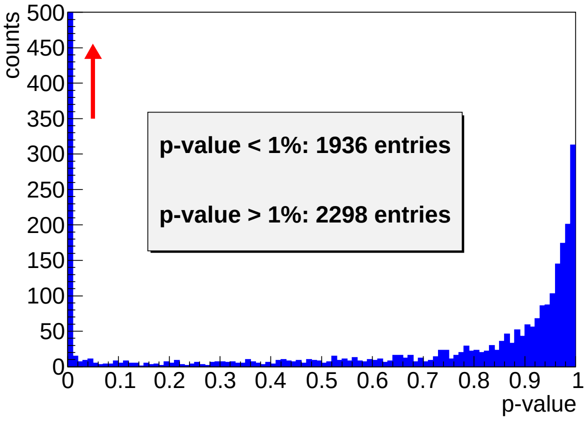

Figure 4.16: P-value distribution for the refit on both $m_{p\pi}$ and $d_{p\pi}$ (ndf $= 2$). The refitted sample was preselected with optimized topological cuts and the corresponding mass cut. The tall peak in the lowest bin indicates the presence of combinatorial background. The rise towards high p-values accounts for the limitation of constraint violation due to cutting.

p-value distribution will deviate from this theoretical picture. For a fake Λ candidate, we expect a large deviation from the constraints. This results in a comparably high shifting effort signalized by large χ^2, i.e. a low p-value. Indeed, we find a very tall peak in the lowest bin of a sample p-value histogram (Fig. 4.16). The input for this refit was preselected with optimized topological cuts (combination 1943, cf. Sec. 4.4.1) and the corresponding mass cut[12] in order to keep the amount of background decent. Actually, this does not only discriminate fake Λ candidates, but also limits the violation of the constraints (i.e. the value of H_1 and H_2) to the respective cut thresholds. Hence, the probability density for χ^2 is shifted towards lower values, which accounts for the rise that we can observe in Fig. 4.16 for high p-values.
This peculiarity of p-value distributions obtained from the kinematic refit leads to the idea of a p-value cut, which is meant to separate the plausible Λ candidates with large p-values from the suspected background. It is implemented as a lower threshold, which we choose to be 40%. Of course, we do not use this cut exclusively, but always apply optimized topological cuts and the mass cut prior to the refit.
As it was mentioned in Sec. 4.5, the kinematic refit can be used in order to improve the resolution of mass spectra of reconstructed particles. If we try this on our Λ spectrum, we have to notice that it does not make sense to apply a mass refit to an experimental mass spectrum, since it will put almost every Λ candidate to

---

[12] I.e. we only take Λ candidates into account which have an invariant mass $m_{p\pi}$ in a range of $\pm 2\sigma$ around the mean of the peak of the topologically cut spectrum.

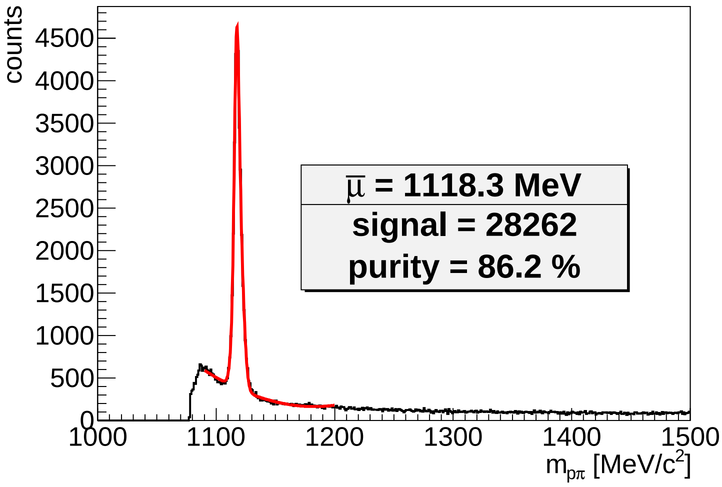

Figure 4.17: $d_{p\pi}$-refitted Λ candidate mass spectrum with optimized topological cuts applied prior to the refit. There is no fundamental difference to the original spectrum (Fig. 4.11). However, the signal is slightly higher, but the purity has decreased.

the literature mass (cf. Fig. 4.14a). Therefore, we can only use the refit on $d_{p\pi}$. The result, which is shown in Fig. 4.17, does not show a fundamental difference in comparison to the original spectrum in Fig. 4.11. However, the signal has increased somewhat at the expense of a reduced purity. This is considered to be a consequence of a general shift of Λ candidates inside the mass cut, but with a larger contribution from fakes.

4.6 $p\Lambda$ Correlation Analysis

The correlation analysis for protons and Λ hyperons confines the set of Λ hyperons established in Sec. 4.4 further, because it can only make use of events which contain both a Λ *and* a proton. We are thus left with an amount of only 2976 viable events. This section only makes use of the topological cuts (cf. Sec. 4.4.1), whereas the influence of the refit will be discussed in Ch. 5.

The analysis is conducted using a *mixed event approach*. This method basically uses the definition of a correlation function given in Eq. 3.7, but since we naturally may have some correlation in *all* of our $p\Lambda$ events (“same events”), we have to emulate entirely uncorrelated $p\Lambda$ pairs. As particles from different events are supposed to have no correlation at all, we combine protons and Λs to so-called “mixed events”.

In order to assure a certain plausibility for those events, we do not randomly mix particles, but categorize them into “mixing bins”, on which the procedures are exe-

property	domains
multiplicity	≤ 3 ≥ 4
primary vertex z	below -62 mm -62 to -44 mm -44 to -26 mm -26 to -8 mm above -8 mm

Table 4.5: Mixing domains for event multiplicity and primary vertex position along the beam axis. There is a total of $2 \times 5 = 10$ mixing bins.

cuted separately. The mixing bins consist of disjoint domains for event multiplicity and primary vertex position along the beam axis (see Tab. 4.5). Each bin is filled with same events until it reaches a size[13] of 10. Then every proton i is combined with every Λ hyperon j, yielding the original 10 same events ($i = j$) and $10 \times 10 - 10 = 90$ mixed events ($i \neq j$).
Since it is the abscissa of the desired correlation function $C(k)$, we need to calculate the center-of-momentum-frame one particle momentum k of every $p\Lambda$ pair (cf. Sec. 3.5). It can be obtained as the magnitude of the 3-momentum $k = |\vec{p}^*|$ of either particle after a Lorentz boost $p^* = B_{\vec{\beta}} p$ into the center of momentum system with

$$\vec{\beta} = \frac{\vec{p}_{p\Lambda}}{E_{p\Lambda}} = \frac{\vec{p}_p + \vec{p}_\Lambda}{E_p + E_\Lambda}. \tag{4.37}$$

These k values are collected from all mixing bins and filled into two separate histograms, one for same events and one for mixed events (see Fig. 4.18). Following Eq. 3.7, we divide the same event histogram by the one for mixed events to obtain the actual correlation histogram. As the theory function Eq. 3.11 suggests (cf. Fig. 3.6), we expect no correlation for high relative momenta, i.e. $C(k) \overset{k\to\infty}{\longrightarrow} 1$. However, we anticipate to have about nine times as many mixed as same events, so some normalization has to be done. Assuming no more relevant effects above $k = 120$ MeV[14], we scale the correlation histogram so that the mean value between 120 MeV and 300 MeV equals 1.
The procedure described above leads to the histogram given in Fig. 4.19. It is fitted in the range $0 \text{ MeV} \leq k \leq 250$ MeV with the theory function given in Eq. 3.11, yielding a source size of

$$r_0 = (0.94 \pm 0.06) \text{ fm}. \tag{4.38}$$

---

[13] After the last event of the data set is reached, partially filled bins are processed as well in order not to lose any data.

[14] Empirical value.

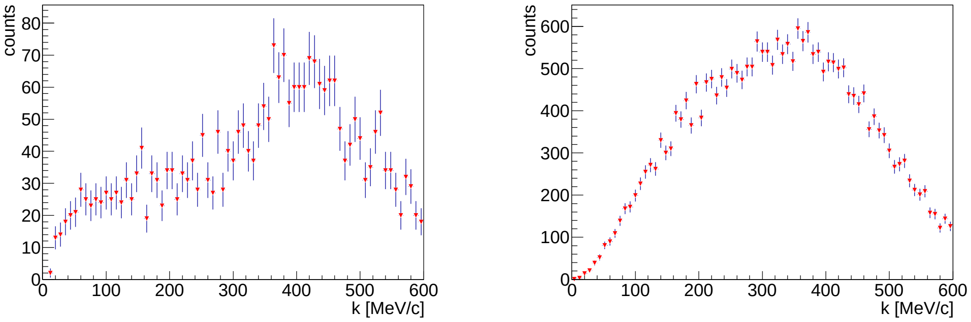

(a)

(b)

Figure 4.18: Relative momentum k histograms of same (left) and mixed (right) $p\Lambda$ events. There is a multiple of entries for mixed events, which makes this histogram appear smoother. We can observe a lack of statistics at very low and high k.

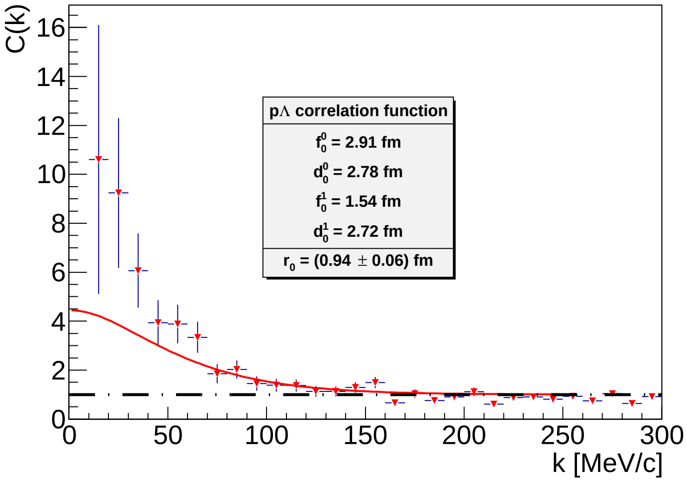

Figure 4.19: Correlation histogram of protons and Λ hyperons. It is fitted with Eq. 3.11 and the fixed parameters from Tab. 3.3, which yields an effective size $r_0 = (0.94 \pm 0.06)$ fm for the $p\Lambda$ source. However, errors get very large for low relative momenta k due to low statistics (cf. Fig. 4.18).

Chapter 5

Results and Discussion

This chapter reviews the results of the experimental analysis and discusses peculiarities and possible adjustments.

5.1 Lambda Reconstruction

The method of topological cuts is a well-proven tool for particle reconstruction, so it is not surprising that it works out quite well in our analysis, too. However, there is one conspicuous feature appearing throughout the analysis, which is the determination of the Λ mass to a value above the literature value of 1115.683 MeV (see Fig. 4.5, 4.11 and 4.17).

This may be an effect of incorrect energy loss correction. The HYDRA framework [23], which is used for the detector-related parts of the analysis, includes utilities to estimate the amount of energy a particle has lost on its way to the detector due to interaction with the target, detector components etc. Depending on the track parameters and the species of the particle, there is a certain amount of momentum added to the measurement. As everyday materials, like metal and plastic, are governed by the electromagnetic interaction, the energy loss will be considerably higher for charged particles like protons and pions. However, the proton and π^- from a Λ decay will usually form *behind* the target, which is transited by the Λ hyperon almost non-dissipative. Hence, the correction applied to them will be too high. This overestimation propagates to the invariant mass $m_{p\pi}$, which eventually explains our findings.

It is explained in Sec. 3.2 that a Λ hyperon is always produced in company with a kaon. It is therefore a legitimate objection, why we do not search for kaons as indicators for strangeness events.

However, the kaon analysis turns out to be even more demanding than the Λ analysis. There are two types of kaons which can appear in Λ reactions, K^+ and K^0. Neutral kaons do not appear as physical particles, but can be described as a superposition of K^0_L ('K long') and K^0_S ('K short'). These CP eigenstates have very similar masses, but highly differing mean lifetimes (by three orders of magnitude!). With a $c\tau$ of over 15 m, the neutral K^0_L will pass the detector undetected, while K^0_S decays very close

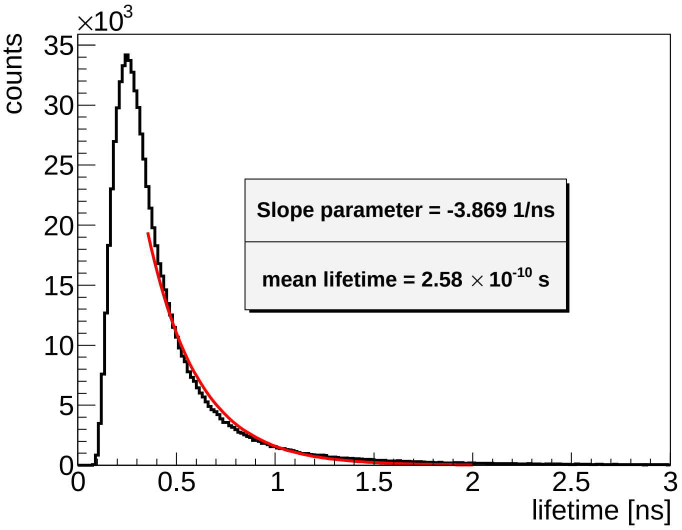

Figure 5.1: Histogram of Λ candidate lifetimes after $l > 42.5$ mm cut. The cutoff for low lifetimes is due to this limitation. From the slope parameter of the exponential fit, a mean lifetime of 2.58×10^{-10} s is calculated. The literature value is $\tau_\Lambda = 2.631(20) \times 10^{-10}$ s.

to the primary vertex ($c\tau = 2.7$ cm) into two pions. The detection of a $pK\Lambda$ event would thus require a multiplicity of 5, which is problematic in the context of detector acceptance. The K^+ on the other hand could be detected as usual charged particles, but it is very difficult to differentiate between them and the neighboring protons and π^+ (cf. Fig. 4.1). On the whole, the requirement of a kaon in Λ events would severely reduce the anyway scarce number of Λ hyperons and the kaon analysis goes beyond the scope of this thesis.

Although we have pointed out certain weaknesses of our Λ sample, it is still qualified to conduct further analyses on the Λ hyperon. As a demonstration, we will determine the Λ mean lifetime.

The lifetime $t_{p\pi}$ of a Λ candidate can be expressed through the primary-secondary-vertex distance l, the momentum $|\vec{p}_{p\pi}|$ and the invariant mass $m_{p\pi}$ (cf. Eq. 4.7):

$$t_{p\pi} = \frac{l}{c} \frac{m_{p\pi}}{|\vec{p}_{p\pi}|} \tag{5.1}$$

This quantity is supposed to follow an exponential function $f(t_{p\pi}) \propto \exp\left(-t_{p\pi}/\tau_{p\pi}\right)$ with the Λ candidates' mean lifetime $\tau_{p\pi}$. Fitting the experimental histogram in Fig. 5.1 yields $\tau_{p\pi} = 2.58 \times 10^{-10}$ s. It has been created using only the cut on $l > 42.5$ mm, since the full set of cuts would deform the distribution too much. Our result resembles the literature value for the Λ hyperon $\tau_\Lambda = 2.631(20) \times 10^{-10}$ s.

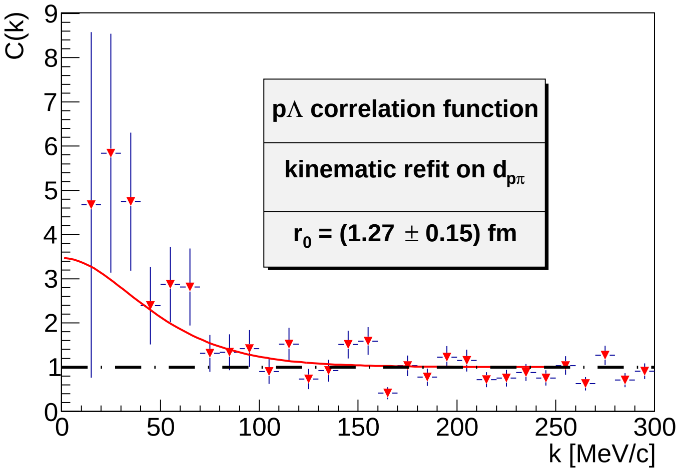

Figure 5.2: Fitted $p\Lambda$ correlation histogram after kinematic refit on $d_{p\pi}$. Compared to the original in Fig. 4.19, there are higher uncertainties and more fluctuations for the rather uncorrelated range above $k = 120$ MeV. The $p\Lambda$ source size retrieved from the fit is $r_0 = (1.27 \pm 0.15)$ fm.

5.2 Kinematic Refit

As already mentioned in the introductory Section 4.5, the kinematic refit works very well, when applied to an exclusive analysis (e.g. [27], [29]). However, for our *inclusive* analysis, it has revealed serious disadvantages. The low number of usable constraints and the sensibility to the omnipresent combinatorial background in this kind of analyses will hardly lead to reliably improved results.

Though the introduction of the p-value cut discriminates some background, there is no general statement possible about the impact of refitting on the outcome of the analysis. This is illustrated by the invariant mass spectrum in Fig. 4.17, which does not experience any improvements from the refit on $d_{p\pi}$, whereas the $p\Lambda$ correlation function clearly changes under the same operation. The comparison of the $d_{p\pi}$-refitted Fig. 5.2 to the original correlation function in Fig. 4.19 exposes an enlargement of uncertainties and a higher fluctuation for the rather uncorrelated region above $k = 120$ MeV. This is seen as a consequence of the further reduction of statistics by the p-value cut (from former 2976 to 1523 $p\Lambda$ events) and the non-uniform behavior of refitted tracks with only one constraint. However, we also have lower values in the leading bins, which raises the result for the $p\Lambda$ source size to $r_0 = (1.27 \pm 0.15)$ fm, compared to former $r_0 = (0.94 \pm 0.06)$ fm.

We conclude that the kinematic refit has an observable influence on the analysis results, but for a low number of constraints this will not lead to a reliable improvement.

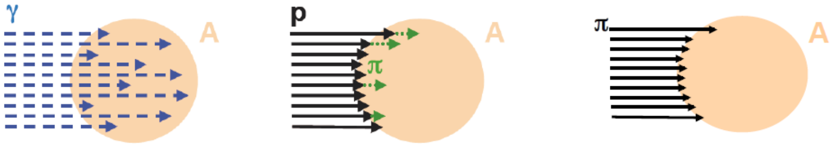

Figure 5.3: In contrast to other bullet particles, pions (on the right) are supposed to interact only on the surface of an atomic nucleus. [30]

Additionally, the p-value cut leads to a reduction of statistics, which is detrimental for analyses that demand a high number of viable events. Nevertheless, if more constraints can be constructed, the kinematic refit might be a useful tool for the analysis of inclusive reactions in the same way as it is for exclusive ones.

5.3 Correlation Analysis

Although the fits of the correlation histograms in Fig. 4.19 and 5.2 appear rather imprecise to the naked eye, they yield $p\Lambda$ source sizes of rather low uncertainty. However, already the disparity of the original and the refitted result shows that these values have to be treated with caution. The correlation analysis is a highly sensitive experimental technique, which incorporates uncertainties from various sources, e.g. the impurities of the particle sets from both PID and of the reconstructed Λ hyperons, the general measurement uncertainties of the particle detector and the approximations made for the theoretical models. In general, all of these influences have to be included into the error of the final result, but this goes beyond the scope of this thesis.

As already mentioned in various places, a correlation analysis is also very dependent on a high number of usable events, because the correlation of interest usually shows in the region of low relative momenta, where we naturally find only a minority of the events (cf. 4.18). Hence, it is very challenging to measure baryon correlations in a pion-induced reaction as we do, because the necessary release of *two* baryons from the nucleus, of which only *one* is involved in the actual inelastic reaction, is a rather improbable event.

However, exactly this peculiarity of pion-induced reactions is a very interesting feature of our analysis and can be related to our findings. As indicated in Fig. 5.3, pions are supposed to interact only directly on the surface of a nucleus, whereas other particles may penetrate further. The consequence is a very localized source for pion-induced particle emissions from a nucleus. In fact, this is consistent with our result of $r_0 \approx 1$ fm, since that is rather comparable to a single surface nucleon being hit by the pion, than to the dimension of a whole tungsten nucleus (~ 6 fm $\approx \sqrt[3]{A(\mathrm{W})}$).

Chapter 6

Outlook

For a continued occupation with the kinematic refit in the context of inclusive analyses, it is mandatory to extend it to the concept of “unknown parameters”, which already has been mentioned in Sec. 4.5.2. It can be used to treat the Λ decay vertex as an individual point in space rather than just a function of the daughter tracks. Thus, the third constraint from 4.28, which is the constraint on the angle α between Λ candidate momentum and the vector pointing from primary to secondary vertex, becomes feasible. The increased number of degrees of freedom for the refit will improve its reliability and functioning.

Concerning the $p\Lambda$ correlation analysis, an important next step is the implementation of various corrections that mainly account for technical issues of the detection process. For instance, an examination of track merging effects can be performed. This refers to the case when two particles hit the detector very close to each other, so that the electronic signals inside the MDCs can interfere, which may lead to fake correlation effects. Another point is the purity of primary PID cuts. So far, we mainly relied on the MDC energy loss measurements. However, we can include other components of the HADES detector, e.g. the META system, in order to improve particle identification. This is in particular important for the differentiation of light particles, like pions, muons and electrons.

In general, an extensive study on statistical and systematical measurement uncertainties has to be performed, since this is a basic requirement for valid scientific results.

Appendix A

Analytical vertex calculation for multiple tracks

This appendix describes a method to calculate an analytical vertex approximation for an arbitrary number of particle tracks. The situation is depicted in Fig. A.1.
In the following, we enumerate tracks by an index $i = 1, 2, ...$ and specify them by a base $\vec{b}_i$ and a unit direction $\hat{d}_i$ with $|\hat{d}_i| = 1$. The vertex position, which will be optimized, is $\vec{r}$.
The perpendicular of the vertex towards any track i (i.e. its distance to that track) forms a right triangle consisting of the catheti d_i and s_i and the hypotenuse v_i. The Pythagorean theorem states

$$s_i^2 = v_i^2 - d_i^2. \tag{A.1}$$

$v_i = |\vec{v}_i|$ can be expressed as the modulus of the vector $\vec{v}_i \equiv \vec{r} - \vec{b}_i$. d_i is the projection of $\vec{v}_i$ onto the track, which can be written as the scalar product $d_i = \hat{d}_i \cdot \vec{v}_i$.

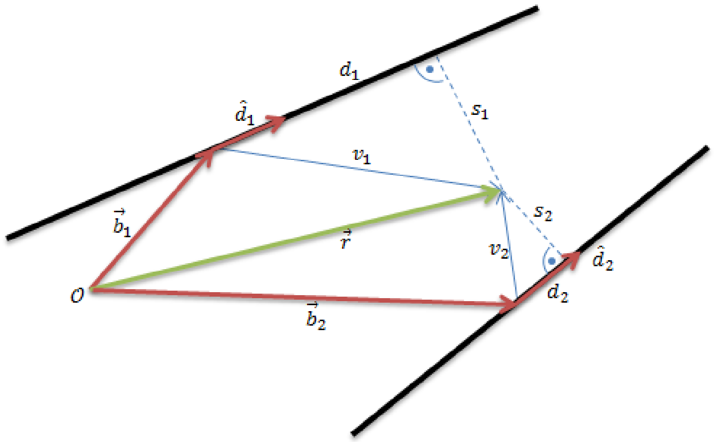

Figure A.1: Illustration of the geometry of the vertex reconstruction problem. For simplicity, only two particle tracks (black lines) are shown, specified by their base $\vec{b}_i$ and direction $\hat{d}_i$. The vertex position, which will be optimized, is $\vec{r}$.

Using the possibility to write any scalar product $\vec{a} \cdot \vec{b} = \vec{b} \cdot \vec{a}$ as a matrix product $\vec{a}^T \vec{b} = \vec{b}^T \vec{a}$ and the associativity of matrix multiplication, we obtain

$$\begin{aligned} s_i^2 &= v_i^2 - d_i^2 = \vec{v}_i^2 - (\hat{d}_i \cdot \vec{v}_i)^2 = \vec{v}_i^T \vec{v}_i - (\vec{v}_i^T \hat{d}_i)(\hat{d}_i^T \vec{v}_i) \\ &= \vec{v}_i^T \vec{v}_i - \vec{v}_i^T (\hat{d}_i \hat{d}_i^T) \vec{v}_i = \vec{v}_i^T (1 - \hat{d}_i \hat{d}_i^T) \vec{v}_i. \end{aligned} \tag{A.2}$$

We now define the matrices $\boldsymbol{M}_i \equiv 1 - \hat{d}_i \hat{d}_i^T$. They are symmetrical and positive semidefinite. With this definition it is obvious, that s_i^2 is a quadratic form of $\vec{v}_i$:

$$s_i^2 = \vec{v}_i^T \boldsymbol{M}_i \vec{v}_i \tag{A.3}$$

Summing over all tracks, we now define the quantity

$$S^2 \equiv \sum_i s_i^2, \tag{A.4}$$

which is a quadratic form as well.
Because of the positive semi-definiteness of each s_i^2, S^2 has a lower bound and can thus be minimized (even though the minimum is in general not unique, see below). We regard a vertex position minimizing S^2 (i. e. the square sum of the distances to all tracks) as optimal.
The minimum of a positive semi-definite quadratic form is found by reducing its gradient to zero (we use $\vec{v}_i = \vec{r} - \vec{b}_i \Rightarrow \partial \vec{v}_i / \partial \vec{r} = 1$ for all i and the chain rule):

$$0 \overset{!}{=} \frac{\partial S^2}{\partial \vec{r}} = \sum_i \frac{\partial s_i^2}{\partial \vec{r}} = \sum_i \underbrace{\frac{\partial \vec{v}_i}{\partial \vec{r}}}_{=1} \frac{\partial s_i^2}{\partial \vec{v}_i} = \sum_i \frac{\partial (\vec{v}_i^T \boldsymbol{M}_i \vec{v}_i)}{\partial \vec{v}_i} = \sum_i 2 \boldsymbol{M}_i \vec{v}_i \tag{A.5}$$

This is a linear equation system for $\vec{r}$:

$$0 = \sum_i \boldsymbol{M}_i \vec{v}_i = \sum_i \boldsymbol{M}_i (\vec{r} - \vec{b}_i) \quad \Rightarrow \quad \left(\sum_i \boldsymbol{M}_i \right) \vec{r} = \sum_i \boldsymbol{M}_i \vec{b}_i \tag{A.6}$$

If $\sum_i \boldsymbol{M}_i$ is invertible, which is the case for two non-parallel tracks and shall be the subject of further investigations for higher track numbers (in practice it has proven to be virtually always invertible), we obtain the unique, analytical vertex $\vec{r}$ as

$$\vec{r} = \left(\sum_i \boldsymbol{M}_i \right)^{-1} \left(\sum_i \boldsymbol{M}_i \vec{b}_i \right). \tag{A.7}$$

This procedure does not take possible uncertainties of the track parameters $\vec{b}_i$ and $\hat{d}_i$ into account. However, if those can be neglected or are not of interest, the given formula provides a very fast (linear order in the number of tracks!) way to calculate vertices.
The distribution of primary vertices calculated with this method is shown in Fig. A.2.

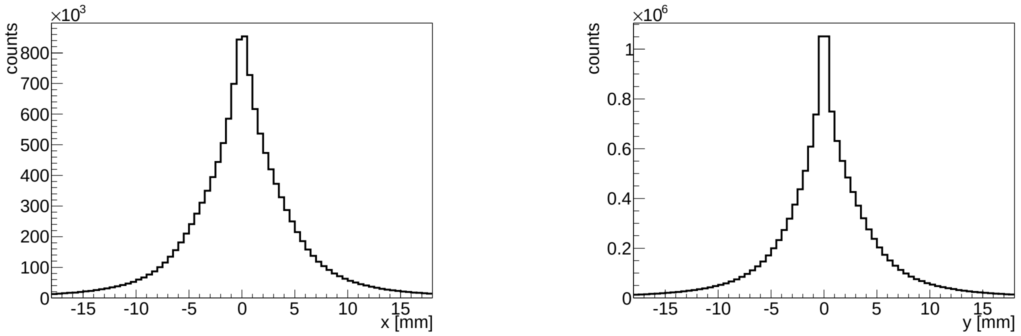

(a) x distribution

(b) y distribution

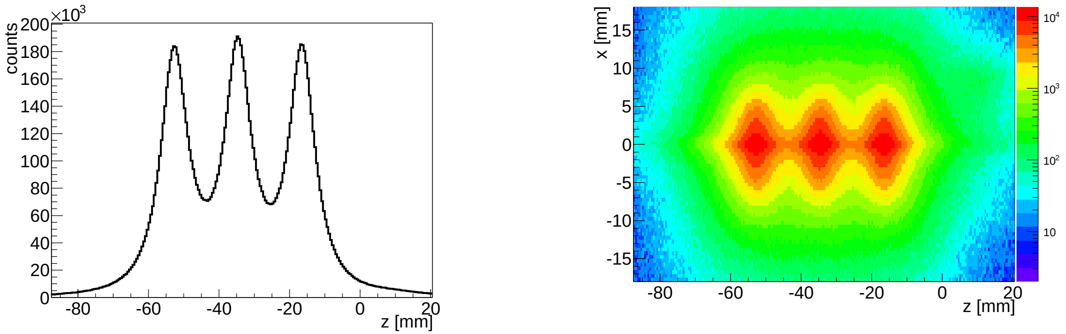

(c) z distribution (beam direction)

(d) In the x-z distribution, the three targets are clearly visible.

Figure A.2: Illustration of the 3-dimensional primary vertex distribution, calculated with the method described in App. A.

Bibliography

[1] PB Demorest, Tim Pennucci, SM Ransom, MSE Roberts, and JWT Hessels. A two-solar-mass neutron star measured using shapiro delay. *Nature*, 467(7319):1081–1083, 2010.

[2] Dany Page. picture, 2009.

[3] Jorge Piekarewicz. The nuclear physics of neutron stars. *Rev. Mex. Fıs. S*, 54(3):104–109, 2008.

[4] Alessandro Drago, Andrea Lavagno, and Giuseppe Pagliara. Can very compact and very massive neutron stars both exist? *Phys. Rev. D*, 89:043014, Feb 2014. URL: `http://link.aps.org/doi/10.1103/PhysRevD.89.043014`, `doi:10.1103/PhysRevD.89.043014`.

[5] Torsten Dahms. Ultrarelativistic heavy-ion collisions, 2014. URL: `http://www.e12.ph.tum.de/~tdahms/Lectures/WS2014-15_QGP/tdahms_qgp_ws2014_01.pdf`.

[6] J. Haidenbauer, S. Petschauer, N. Kaiser, U.-G. Meißner, A. Nogga, and W. Weise. Hyperon–nucleon interaction at next-to-leading order in chiral effective field theory. *Nuclear Physics A*, 915:24 – 58, 2013. URL: `http://www.sciencedirect.com/science/article/pii/S0375947413006167`, `doi:http://dx.doi.org/10.1016/j.nuclphysa.2013.06.008`.

[7] K. A. Olive et al. Review of Particle Physics. *Chin. Phys.*, C38:090001, 2014. `doi:10.1088/1674-1137/38/9/090001`.

[8] G Agakichiev, C Agodi, H Alvarez-Pol, E Atkin, E Badura, A Balanda, A Bassi, R Bassini, G Bellia, D Belver, et al. The high-acceptance dielectron spectrometer hades. *The European Physical Journal A*, 41(2):243–277, 2009.

[9] J Michel, M Böhmer, M Kajetanowicz, G Korcyl, L Maier, M Palka, J Stroth, A Tarantola, M Traxler, C Ugur, and S Yurevich. The upgraded hades trigger and data acquisition system. *Journal of Instrumentation*, 6(12):C12056, 2011. URL: `http://stacks.iop.org/1748-0221/6/i=12/a=C12056`.

[10] KClus group, Technische Universität München. Pion beam experiment with hades, 2015. URL: `https://www.e12.ph.tum.de/groups/kcluster/ResearchTopic5.php`.

[11] Trassiorf. Premier octet de baryons, 2007. URL: `https://commons.wikimedia.org/wiki/File:Baryon-octet.svg`.

[12] R Machleidt and I Slaus. The nucleon-nucleon interaction. *Journal of Physics G: Nuclear and Particle Physics*, 27(5):R69, 2001.

[13] W Brückner, MA Faessler, TJ Ketel, K Kilian, J Niewisch, B Pietrzyk, B Povh, HG Ritter, M Uhrmacher, P Birien, et al. Spin-orbit interaction of lambda particles in nuclei. *Physics Letters B*, 79(1):157–160, 1978.

[14] Peter Weinberger. Revisiting louis de broglie's famous 1924 paper in the philosophical magazine. *Philosophical magazine letters*, 86(7):405–410, 2006. URL: `http://dx.doi.org/10.1080/09500830600876565`, `arXiv:http://dx.doi.org/10.1080/09500830600876565`, `doi:10.1080/09500830600876565`.

[15] Bernhard Lippmann and Julian Schwinger. Variational principles for scattering processes. i. *Phys. Rev.*, 79:469–480, Aug 1950. URL: `http://link.aps.org/doi/10.1103/PhysRev.79.469`, `doi:10.1103/PhysRev.79.469`.

[16] J. J. Sakurai. *Modern Quantum Mechanics*. 1994.

[17] Robert Hanbury Brown and Richard Q. Twiss. Correlation between photons in two coherent beams of light. 1956. `doi:10.1038/177027a0`.

[18] Gerson Goldhaber, Sulamith Goldhaber, Wonyong Lee, and Abraham Pais. Influence of bose-einstein statistics on the antiproton-proton annihilation process. *Phys. Rev.*, 120:300–312, Oct 1960. URL: `http://link.aps.org/doi/10.1103/PhysRev.120.300`, `doi:10.1103/PhysRev.120.300`.

[19] W Bauer, C Gelbke, and S Pratt. Hadronic interferometry in heavy-ion collisions. *Annual Review of Nuclear and Particle Science*, 42(1):77–98, 1992. URL: `http://dx.doi.org/10.1146/annurev.ns.42.120192.000453`, `arXiv:http://dx.doi.org/10.1146/annurev.ns.42.120192.000453`, `doi:10.1146/annurev.ns.42.120192.000453`.

[20] Stefan Petschauer. Chiral su(3)-dynamics and baryon-baryon interactions, 2011. URL: `http://www.t39.ph.tum.de/T39_files/T39_people_files/petschauer_files/diploma_thesis.pdf`.

[21] J. Adams et al. Proton-Λ correlations in central au+au collisions at $\sqrt{s_{NN}} = 200$ gev. *Phys. Rev. C*, 74:064906, Dec 2006. URL: `http://link.aps.org/doi/10.1103/PhysRevC.74.064906`, `doi:10.1103/PhysRevC.74.064906`.

[22] R. Lednicky and V. L. Lyuboshits. Final State Interaction Effect on Pairing Correlations Between Particles with Small Relative Momenta. *Sov. J. Nucl. Phys.*, 35:770, 1982. [Yad. Fiz.35,1316(1981)].

[23] HADES collaboration. Hydra - the hades analysis package reference guide, 2015. URL: `http://web-docs.gsi.de/~halo/docs/hydra/classDocumentation/dev/index.html`.

[24] Hans Bethe. Theory of the passage of fast corpuscular rays through matter. *Annalen Phys.*, 5:325–400, 1930.

[25] Lev Landau. On the energy loss of fast particles by ionization. *J. Phys.(USSR)*, 8:201–205, 1944.

[26] Barbara Schweißhelm. private communication, 2015.

[27] Dominik Pleiner. Hunting the ppk^-: A kinematic refit for the exclusive analysis of the reaction $pp \rightarrow pK^+\Lambda$, 2012. URL: `https://www.e12.ph.tum.de/groups/kcluster/Documents/Publications/Thesis_Pleiner.pdf`.

[28] Paul Avery. Fitting theory writeups and references, 1998. URL: `www.phys.ufl.edu/~avery/fitting.html`.

[29] Johannes Siebenson. Exclusive analysis of the $\Lambda(1405)$ resonance in the charged $\Sigma\pi$ decay channels in proton proton reactions with hades, 2010. URL: `https://www.e12.ph.tum.de/groups/kcluster/Documents/Publications/Johannes_Siebenson.pdf`.

[30] Laura Fabbietti. Pion induced reactions: strangeness programme. In *Achievements and Perspectives in Low-Energy QCD with Strangeness*, 2014.

Danksagung

Zum Abschluss dieser Arbeit möchte ich noch ein paar persönliche Worte auf Deutsch schreiben, um die zahlreichen Personen zu würdigen, die direkt oder indirekt zum Gelingen dieses Projektes beigetragen haben.
Zuvorderst gilt meine Dankbarkeit meinem Betreuer Oliver Arnold, der mir mit einer unvergleichlichen Ruhe zu jeder meiner zahllosen Fragen eine Antwort gab oder recherchierte. Auch in schwierigen Situationen hatte er immer einen Ratschlag für mich bereit und oft war es sein Verdienst, dass ich Phasen mangelnder Motivation überwinden konnte.
Nicht weniger Dank gilt Prof. Dr. Laura Fabbietti, die mich herzlich und unkompliziert als zeitweiliges Mitglied ihrer Arbeitsgruppe aufgenommen hat und mir somit die Möglichkeit gab, diese Arbeit anzufertigen. Trotz ihrer Auslastung durch eigene Termine fand sie regelmäßig Zeit, um sich dem Arbeitsfortschritt ihrer Bacheloranden zu widmen, und gab uns damit das beruhigende Gefühl, dass wir ihr am Herzen liegen.
Viele erfreuliche und erstaunliche Momente durfte ich mit meinen Bürokameraden erleben. Insbesondere möchte ich Barbara danken, mit der viel "Leid" durch Teilen zu halbem Leid wurde, da wir uns stets in ähnlichen Situation befanden. Auch ohne Renate hätte etwas gefehlt, denn sie konnte uns alle stets zum Lachen bringen, wenn Unmut drohte.
An dieser Stelle möchte ich auch Torsten und Robert würdigen, die ich zahlreiche Male für mich in Beschlag nehmen durfte, nachdem sie sich um ihre eigenen Schützlinge gekümmert hatten. Auch den Rest der Arbeitsgruppe werde ich in sehr guter Erinnerung behalten, denn ich entsinne mich keiner Mittagspause, keiner Kuchensession, keines Groupmeetings ohne Lachen und den ein oder anderen Unfug. Von den Festen und Ausflügen ganz zu schweigen.
Zu guter Letzt danke ich natürlich allen meinen Freunden und insbesondere meiner lieben Familie, meinen Eltern und meiner Schwester dafür, dass sie mir auch eine schöne Welt abseits von Bachelorarbeit, Uni und Physik bereitet haben, in die ich bei Bedarf immer ausweichen konnte.
Danke!